

Kinematic cosmic dipole from a large sample of strong lenses

Martin Millon,^a Charles Dalang,^b Thomas Collett,^c Camille Bonvin^a

^aDépartement de Physique Théorique, Université de Genève,
24 quai Ernest-Ansermet, CH-1211 Genève 4, Switzerland

^bInstitut Philippe Meyer, Département de Physique, Ecole Normale Supérieure (ENS),
Université PSL, 24 Rue Lhomond, F-75231, Paris, France

^cInstitute of Cosmology and Gravitation, University of Portsmouth,
Burnaby Road, Portsmouth PO1 3FX, UK

E-mail: martin.millon@unige.ch, charles.dalang@phys.ens.fr,
thomas.collett@port.ac.uk, camille.bonvin@unige.ch

Abstract. Measurements of the kinematic cosmic dipole continue to show an intriguing tension between the value inferred from the CMB and that obtained from high-redshift source number counts. While the measured dipole direction appears consistent, the amplitude, set by the observer’s peculiar velocity v_o , remains in significant disagreement. In this paper, we propose using strong gravitational lenses with well-measured Einstein radii to estimate the kinematic cosmic dipole, through the relativistic distortion of the Einstein angle induced by the observer’s motion. We show that this effect could be detected solely from measurements of the Einstein radius in wide, high-resolution imaging surveys such as Euclid. However, the precision achievable using Einstein-radius measurements alone, without redshift or lens-galaxy mass information, appears insufficient to discriminate between the CMB value of v_o and that derived from source number counts at high statistical significance. Nevertheless, we demonstrate that including a large sample of lenses with available kinematic information, either via the Fundamental Plane relation or, ideally, through spectroscopic velocity-dispersion measurements, drastically reduces the noise and substantially improves the constraining power of this method. We show that, for a realistic sample of strong lenses detected by Euclid and complemented with spectroscopic velocity dispersion measurements from 4MOST or DESI, it is possible to discriminate between the CMB- and source-number-counts-inferred values at the $\sim 4\sigma$ level using a new, fully independent method. We further demonstrate that this technique is only weakly sensitive to strong-lensing selection effects, with selection biases and threshold effects estimated to be well below the 1% level.

Contents

1	Introduction	1
2	Einstein angle aberration	3
3	Measurement of the observer velocity from lensing alone	6
3.1	Likelihood definition	6
3.2	Lens population model	6
3.3	Lensing only results	7
4	Combining lensing and Stellar Kinematics	9
4.1	Spectroscopic velocity dispersion	9
4.2	Fundamental Plane	11
4.3	Euclid Forecast	12
5	Discussion	15
6	Conclusion	19
A	Calculation of the mean Einstein radius integrated over redshifts	20
B	Impact of the selection function on the dipole	22
C	Simulation of the Fundamental Plane observables	25
D	Observer velocity effect on the Fundamental Plane observables	27

1 Introduction

Using measurements of the dipole anisotropy in the blackbody temperature of the Cosmic Microwave Background (CMB), the *Planck* satellite has accurately determined both the magnitude and direction of the observer’s velocity. The observer’s motion produces a temperature modulation of order $\delta T/\langle T \rangle \sim \mathcal{O}(10^{-3})$ around the angularly averaged temperature $\langle T \rangle$. This effect allows for a precise measurement of the observer’s velocity, with magnitude $v_o = 369.82 \pm 0.11 \text{ km s}^{-1}$, directed towards $\hat{v}_o = (264.021^\circ \pm 0.011^\circ, 48.253^\circ \pm 0.005^\circ)$ in Galactic coordinates [1–4]. This interpretation is valid under the assumption that the intrinsic CMB dipole due to primordial density perturbations, expected to be of order $\mathcal{O}(10^{-5} - 10^{-6})$, is small in comparison.

The observer’s velocity also introduces two other signatures in the CMB: a Doppler *modulation* effect, which amplifies the apparent temperature fluctuations in the velocity direction and reduces them in the opposite direction, and an *aberration* effect, which changes the angular scales of the temperature fluctuations. These two effects induce correlations between the l and $l \pm 1$ multipoles of the CMB. Both of these effects have been detected [4–6], leading to results consistent with the velocity inferred from the dipole, and thus supporting the *entirely kinematic* interpretation of the CMB dipole. However, the relatively large error bars still allow for an intrinsic component at the level of $\sim 40\%$ of the CMB dipole [7].

On the other hand, the observer’s velocity can be measured independently using high-redshift source number counts, such as quasars, following a method originally proposed by [8]. The observer velocity generates a dipolar modulation in the source number counts, due both to aberration and to threshold effects, i.e. the fact that sources will appear brighter in the velocity direction, increasing the number of sources above the flux threshold. In such analyzes, it is crucial to consider sources distributed over a sufficiently large cosmological volume in order to minimize contamination from local structures. Recent measurements based on quasar number counts from large imaging surveys point toward a discrepant value of the observer’s velocity, with several analyzes reporting a tension at the level of 3–5.7 σ [9–11]. However, contamination by low-redshift sources affected by local clustering [12] could account for part of this discrepancy. Evolution of the source population was proposed as a possible explanation for the tension [13], until it was shown not to affect the number count dipole, if source properties are measured close to the flux limit [14]. Overall, while measurements based on the QUAIA catalog [15] seem not to support the presence of such a tension [16, 17], a recent re-analysis of the CATWISE data still finds discrepant results at the $\sim 3\sigma$ level, even after accounting for possible local clustering effects [18]. Redshift tomography [19] and measurements of l and $l + 1$ correlations in source number counts [20] were proposed as powerful complementary methods, allowing to cleanly disentangle threshold effects from the observer velocity. A review of the current status of these observations, potential systematics impacting these measurements, and cosmological implication of the CMB dipole anomaly can be found in [21, 22]. This lack of consensus highlights the need for independent methods to measure the observer’s velocity.

In this work, we propose an independent measurement of the observer’s peculiar velocity using strong gravitational lenses. Our method relies solely on angular measurements on the sky, providing a very robust way of extracting the observer velocity. The observable is derived purely from special relativity: a non-comoving observer perceives relativistic aberration, which induces a direction-dependent modulation of the observed Einstein radius. We demonstrate that selection effects, that modulate the number of detected Einstein rings across the sky, have a completely negligible impact on the measured dipole, below 0.1%. As such, this observable is insensitive to flux-related and clustering systematics that may bias source-count dipole experiments. This measurement, however, requires a very large number of strong gravitational lenses to detect a small distortion of the Einstein ring for lenses aligned with the observer velocity.

Euclid is expected to find about $\mathcal{O}(10^5)$ strong gravitational lenses by the end of the mission, a 2 order of magnitude increase compared to the $\mathcal{O}(10^3)$ lenses known from Stage-III imaging surveys. Already in the first Q1 data release, covering only 63 square-degrees, Euclid has revealed 497 high-quality new lens candidates [23] thanks to the combination of computer vision methods and human visual inspection [24–26]. According to [23], this is expected to scale to approximately 7,000 new strong lenses in the first Euclid data release (DR1) and to more than 10^5 lenses over the entire Euclid Wide survey. In addition, the image quality of Euclid enables very precise measurements of the Einstein angle, at the level of $\sim 1\%$. As we demonstrate in this work, the observer’s peculiar velocity can be extracted using this observable alone. If spectroscopic redshifts for the background sources and the lens galaxy, as well as velocity dispersion information for the lens are available, even for a sub-set of all systems, the precision of the measurement can be significantly improved.

This paper is organized as follows. In Section 2, we derive the equations describing the aberration of the Einstein angle induced by the observer’s velocity in strongly lensed systems.

In Section 3, we introduce the Bayesian framework used to infer the observer’s velocity, present the simulated lens sample used to validate the method, and report the resulting constraints on the dipole amplitude and direction obtained using lensing information alone. In Section 4, we show how additional lens kinematic information, either from spectroscopic measurements or inferred via the Fundamental Plane (FP) relation, can be incorporated into the analysis to improve the constraints. Finally, we conclude and discuss the limitations of the method in Section 5. Throughout the paper, we assume the flat Λ -Cold Dark Matter model with $H_0 = 70 \text{ km s}^{-1} \text{ Mpc}^{-1}$ and $\Omega_m = 0.3$ to convert redshifts into angular diameter distances.

2 Einstein angle aberration

The peculiar velocity of the observer, \mathbf{v}_o , leads to a distortion of the Einstein ring due to aberration, as described in [27, 28]. Consequently, a perfectly circular Einstein ring of radius θ_E will appear to a boosted observer as an ellipse, as shown in Fig. 1. To compute the distortion, without loss of generality, we align the \mathbf{e}_z axis along the observer velocity and we place the direction of the center of mass of the lens $\hat{\mathbf{n}}$ in the $\mathbf{e}_z - \mathbf{e}_y$ plane, as illustrated in Figure 1. A boosted observer will see the center of mass in the direction $\hat{\mathbf{n}}' \neq \hat{\mathbf{n}}$, which however still lies in the $\mathbf{e}_z - \mathbf{e}_y$ plane. The Einstein ring seen by the boosted observer lives in the plane orthogonal to $\hat{\mathbf{n}}'$. To describe its shape, we adopt the same coordinate system as in [28], i.e. we define $\hat{\mathbf{e}}'_1$ along the \mathbf{e}_x direction, such that angles along that axis are preserved under the boost, and $\hat{\mathbf{e}}'_2$ lies in the $\mathbf{e}_z - \mathbf{e}_y$ plane, orthogonally to $\hat{\mathbf{n}}'$. Angles along $\hat{\mathbf{e}}'_2$ are deformed by the boost. We denote by θ_{cm} the angle between \mathbf{v}_o and the unboosted center of mass of the lens, and by θ_{min} and θ_{max} the angle between \mathbf{v}_o and the unboosted extremities of the ring. The impact of the boost on an angle θ , at linear order in v_o/c , is given by

$$\theta' = \theta - \frac{v_o}{c} \sin \theta'. \quad (2.1)$$

With this, we find that the boosted Einstein radius in direction $\hat{\mathbf{e}}'_2$ is given by

$$\theta'_{E2} = \theta'_{\text{max}} - \theta'_{\text{cm}} = \theta_{E2} \left(1 - \frac{v_o}{c} \cos \theta'_{\text{cm}} \right) = \theta'_{\text{cm}} - \theta'_{\text{min}}. \quad (2.2)$$

The fact that the boosted ring remains centered on the boosted center of mass is valid in the limit $\theta_{E2} \ll \theta_{\text{cm}}$. In contrast, in the $\hat{\mathbf{e}}'_1$ direction the boosted Einstein radius is the same as the unboosted one

$$\theta'_{E1} = \theta_{E1}. \quad (2.3)$$

The Einstein angle in an arbitrary direction can be expressed as a function of the azimuthal angle δ' , defined relative to $\hat{\mathbf{e}}'_1$:

$$\begin{aligned} \theta'_E(\delta') &= \sqrt{\theta'_{E1}(\delta')^2 + \theta'_{E2}(\delta')^2} \\ &= \sqrt{\theta_{E1}(\delta')^2 + \theta_{E2}(\delta')^2 \left(1 - \frac{v_o}{c} \cos \theta'_{\text{cm}} \right)^2}. \end{aligned} \quad (2.4)$$

For simplicity, we assume that, for an observer at rest, the Einstein ring is a perfect circle, arising from a spherical mass distribution, such as a Singular Isothermal Sphere (SIS)

$$\theta_{E1}(\delta') = \theta_E \cos \delta', \quad (2.5)$$

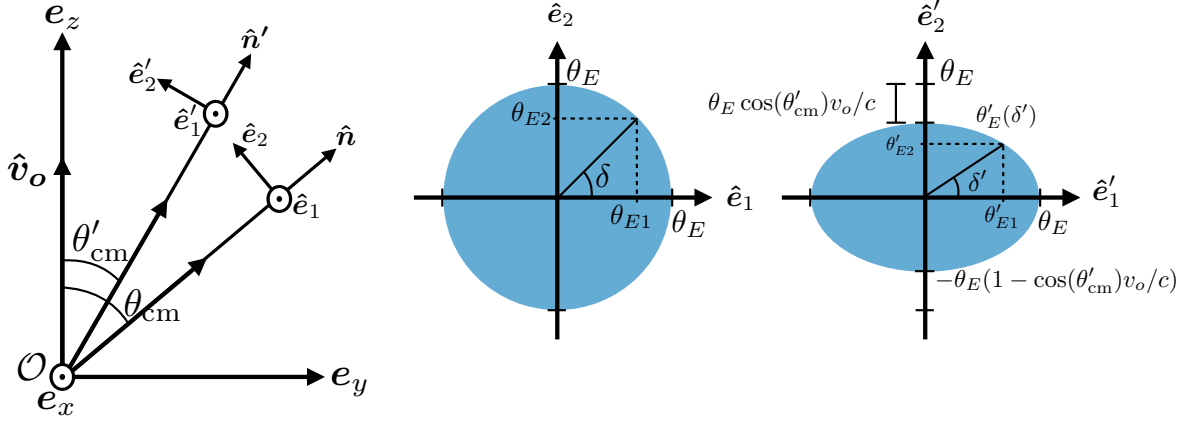


Figure 1. *Left panel:* Coordinate system used in this work. We consider two observers, located at the origin O . The first observer is stationary in this frame and measures comoving quantities, which are written without primes, e.g. θ_{cm} . Because of the symmetry around the e_z axis, the system is fully captured by lenses which lie in the $e_y - e_z$ plane. The stationary observer sees a perfect circular Einstein ring with Einstein angle θ_E in the direction \hat{n} . They associate a coordinate system orthogonal to \hat{n} on the sky $\{\hat{e}_1, \hat{e}_2\}$, depicted in the *middle panel*. This coordinate system is such that the \hat{e}_1 vector is orthogonal both to \hat{n} and v_o (here it is aligned with e_x), while \hat{e}_2 lives in the $e_y - e_z$ plane. The second observer moves with peculiar velocity v_o aligned with \hat{e}_z and observes the Einstein ring in the \hat{n}' direction, which forms an angle θ'_{cm} with the e_z axis. For this moving observer, the Einstein ring appears squashed along the \hat{e}'_2 direction, but unchanged along the \hat{e}'_1 direction. It appears approximately as an ellipse in the coordinate system defined by $\{\hat{e}'_1, \hat{e}'_2\}$, as can be seen in the *right panel*. The Einstein angle as a function of the observed boosted azimuthal angle δ' can be computed from the components $\theta'_{E1}(\delta')$ and $\theta'_{E2}(\delta')$. The amplitude of this deformation is proportional to $\cos(\theta_{\text{cm}})v_o/c$.

$$\theta_{E2}(\delta') = \theta_E \sin \delta'. \quad (2.6)$$

Inserting (2.5) and (2.6) into Eq. (2.4), we can relate the observed Einstein angle $\theta'_E(\delta')$ seen by a moving observer to the comoving one θ_E

$$\theta'_E(\delta') = \theta_E \left(1 - \sin^2 \delta' \frac{v_o}{c} \cos \theta'_{\text{cm}} \right). \quad (2.7)$$

In practice, the Einstein angle is measured by fitting a mass model, e.g. a SIS model, to the imaging data. Consequently, the measured Einstein angle is azimuthally average over δ' :

$$\begin{aligned} \theta'_E &= \frac{1}{2\pi} \int_0^{2\pi} d\delta' \theta_E \left(1 - \sin^2 \delta' \frac{v_o}{c} \cos \theta'_{\text{cm}} \right) \\ &= \theta_E \left(1 - \frac{v_o}{2c} \cos \theta'_{\text{cm}} \right). \end{aligned} \quad (2.8)$$

In the rest of this work, we use the average Einstein angle θ'_E as our primary observable to measure v_o .

To increase the statistics, we measure the mean size of all detected rings in a given solid angle $d\Omega'$. Since the Einstein angle depends on the redshifts of the sources, z'_s , and of the lens, z'_l , this introduces two integrals weighted by the number of systems observed in that solid angle $\frac{dN(\hat{n}', z'_s, z'_l)}{d\Omega' dz'_s dz'_l}$

$$\langle \theta'_E(\hat{n}') \rangle = \left(\frac{dN(\hat{n}')}{d\Omega'} \right)^{-1} \int dz'_s \int dz'_l \frac{dN(\hat{n}', z'_s, z'_l)}{d\Omega' dz'_s dz'_l} \theta'_E(\hat{n}', z'_s, z'_l), \quad (2.9)$$

with

$$\frac{dN(\hat{\mathbf{n}}')}{d\Omega'} = \int dz'_s \int dz'_l \frac{dN(\hat{\mathbf{n}}', z'_s, z'_l)}{d\Omega' dz'_s dz'_l}. \quad (2.10)$$

To evaluate Eq. (2.9), we need to express the Einstein radius as a function of the boosted redshifts z'_s and z'_l , which introduces additional distortions. The Einstein radius depends indeed on the distances to the source and to the lens, and fixed values of z'_s and z'_l correspond to different distances in different directions. As shown in Appendix A, the Einstein radius in redshift space is given by

$$\theta'_E(\hat{\mathbf{n}}', z'_s, z'_l) = \theta_E(r(z'_s), r(z'_l)) \left(1 - \frac{v_o}{2c} \cos \theta'_{\text{cm}}\right) + \left((1+z_s) \frac{\partial \theta_E}{\partial z_s} + (1+z_l) \frac{\partial \theta_E}{\partial z_l} \right) \frac{v_o}{c} \cos \theta'_{\text{cm}}, \quad (2.11)$$

where $\theta_E(r(z'_s), r(z'_l))$ is the unboosted Einstein ring evaluated at the comoving distances $r(z'_s)$ and $r(z'_l)$, which do not depend on direction.¹ From Eq. (2.11) we see that if we would measure the Einstein ring in bins of observed redshifts, the dipolar contribution would be affected by two terms: aberration and distance perturbations. However, once we integrate over all redshifts, the second contribution cancels and only aberration persists. To see this we need to express the number of detected Einstein rings in terms of z'_s and z'_l . The detailed calculation can be found in Appendix A. We obtain

$$\begin{aligned} \frac{dN(z'_s, z'_l, \hat{\mathbf{n}}')}{d\Omega' dz'_s dz'_l} &= \frac{dN(r(z'_s), r(z'_l))}{d\Omega dz_s dz_l} \left(1 + \frac{4v_o}{c} \cos \theta'_{\text{cm}}\right) \\ &+ \left[(1+z_s) \frac{\partial}{\partial z_s} \left(\frac{dN}{d\Omega dz_s dz_l} \right) + (1+z_l) \frac{\partial}{\partial z_l} \left(\frac{dN}{d\Omega dz_s dz_l} \right) \right] \frac{v_o}{c} \cos \theta'_{\text{cm}}. \end{aligned} \quad (2.12)$$

The second line in Eq. (2.12) combines with the $2v_o/c$ in the first line, and with the second term in Eq. (2.11) to give rise to a boundary term, which exactly vanishes (see Appendix A for more detail). Moreover the effect of aberration in the number of detected systems (the remaining $2v_o/c$ in the first line of Eq. (2.12)) cancels in the numerator and the denominator of Eq. (2.9). Due to aberration, we see more Einstein rings per solid angle in the direction of the boost, but since we normalise the Einstein radius by the number of detected Einstein rings, this effect does not impact the final result. With this, we obtain

$$\langle \theta'_E(\hat{\mathbf{n}}') \rangle = \left(1 - \frac{v_o}{2c} \cos \theta'_{\text{cm}}\right) \langle \theta_E \rangle, \quad (2.13)$$

where $\langle \theta_E \rangle$ is the mean Einstein radius of the unboosted sample

$$\langle \theta_E \rangle = \int dz'_s \int dz'_l f(z'_s, z'_l) \theta_E(z'_s, z'_l), \quad (2.14)$$

with $f(z'_s, z'_l)$ the redshift distribution of systems

$$f(z'_s, z'_l) = \frac{\frac{dN(z'_s, z'_l)}{d\Omega dz_s dz_l}}{\int dz'_s \int dz'_l \frac{dN(z'_s, z'_l)}{d\Omega dz_s dz_l}}. \quad (2.15)$$

¹Note that in the second term, we can use interchangeably z or z' since they multiply a term which is already linear in v_o/c

Eq. (2.13) allows us to measure the observer velocity v_o by fitting a monopole term, proportional to the mean of the lens sample $\langle\theta_E\rangle$ and a dipole term proportional to v_o . This relies on the underlying assumptions that there are no selection effects, i.e. that all systems are detected. In Section 5, we will relax this assumption, introducing a selection in flux and in size. We will show that this introduces additional contributions to the dipole, which are however much smaller than the effect of aberration. More precisely the selection in size introduces a contamination of the order of 0.1% while the selection in flux is three orders of magnitude smaller. This shows that Einstein rings provide a very robust observable to measure the observer velocity, without being contaminated by selection effects that are typically difficult to characterize.

Note that Eq. (2.13) has been derived in redshift space, since the source and lens redshifts can be measured. However, since we integrate over all systems, we could have instead chosen to integrate over comoving distances r_s and r_l , without changing the result. In this case, the Einstein radius is simply given by Eq. (2.8), and the number of systems is only affected by aberration $d\Omega/d\Omega' = 1 + 2\frac{v_o}{c}\cos\theta'_{\text{cm}}$. The final result is then the same as Eq. (2.13), with redshifts replaced by comoving distances.

3 Measurement of the observer velocity from lensing alone

3.1 Likelihood definition

We consider a catalog of N azimuthally averaged Einstein radii measurements θ'_{E_n} with associated galactic coordinates (l_n, b_n) , forming an angle $\theta'_{\text{cm},n}$ with respect to the dipole direction (l_o, b_o) . We define $\langle\theta_E\rangle$ as the mean Einstein radius of the sample, σ_{θ_E} as the standard deviation of the distribution, and $\delta\theta'_{E_n}$ as the associated measurement error for each lens. One can fit a monopole and a dipole by maximizing the likelihood:

$$\ln \mathcal{L}_1 = -\frac{1}{2} \sum_{n=1}^N \frac{\left[\theta'_{E_n} - \langle\theta_E\rangle \left(1 - \frac{v_o}{2c} \cos(\theta'_{\text{cm},n})\right)\right]^2}{\delta\theta'^2_{E_n} + \sigma_{\theta_E}^2} - \frac{1}{2} \sum_{n=1}^N \ln[2\pi(\delta\theta'^2_{E_n} + \sigma_{\theta_E}^2)], \quad (3.1)$$

where $\langle\theta_E\rangle$, σ_{θ_E} , l_o , b_o , and v_o are free parameters.

Here, we fit a displacement of the mean of the Einstein–radius distribution as a function of position on the sky. This probe has the advantage that it does not require any spectroscopic information about the lenses, not even the lens or source redshifts. The measurement relies solely on angle measurements in the plane of the sky. However, the intrinsic scatter of the distribution, σ_{θ_E} , constitutes a significant source of noise, driven primarily by the broad distribution of lens galaxy masses and the wide range of lens and source redshifts. The noise introduced by the unknown lens mass is analogous to the unknown intrinsic shape of the galaxy, introducing shape noise in weak lensing analysis. However, in contrast to weak lensing, the mass of the lensing galaxy can be estimated independently from other techniques. As we demonstrate in Section 4, incorporating spectroscopic redshift information for both the lens and the source, together with independent mass estimates (e.g., from velocity–dispersion measurements or from the FP relation; [29, 30]), can substantially reduce this noise.

3.2 Lens population model

We use the LENSPOP [31, 32] lens simulation package to generate a realistic population of strong lenses expected from Euclid. LENSPOP draws deflector galaxies from the observed

distributions of velocity dispersions and ellipticities measured in the Sloan Digital Sky Survey [33]. Deflectors are assumed to be isothermal and are randomly distributed in comoving volume. Sources are placed behind the deflectors, with source redshifts and luminosities drawn from the catalog of [34], which uses semi-analytic models to populate galaxies onto the dark matter halos of the Millennium Simulation [35].

This procedure results in a population of lenses representative of those present in the Universe; however, for our purposes, we require the subset of lenses that would be *discovered* by Euclid. To this end, LENSPOP simulates observations of this population with Euclid-like data quality and applies a simplified discovery selection function. As described in [32], this selection function can be summarized by requirements on the signal-to-noise ratio of the source, a minimum Einstein radius, a total source magnification greater than 3, and an arc length sufficient for the system to be resolved as an extended object.

The properties of the resulting lens sample are shown in Figure 2. While the simplifying assumptions of LENSPOP cannot perfectly reproduce the true Euclid selection function, they have been shown to accurately predict both the number of galaxy-galaxy lenses discoverable by Euclid and their Einstein radius distribution [23, 36]. These are precisely the quantities that must be modeled reliably for our cosmic dipole inference forecast to be robust.

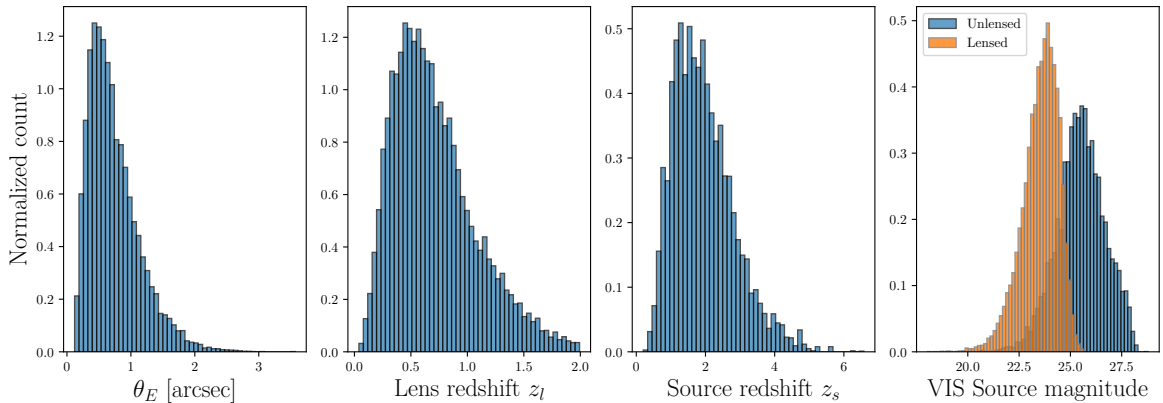


Figure 2. Properties of the simulated Euclid lens sample considered in this work.

From this sample, we randomly assign galactic coordinates (l_n, b_n) to each lens in the catalog within a footprint that mimics the Euclid Wide Survey footprint, requiring $|b_n| > 30^\circ$. We simulate the observed θ'_{E_n} from the true θ_{E_n} using Eq. (2.8) and adding Gaussian noise with standard deviation $\delta\theta'_{E_n}/\theta'_{E_n} = 0.02$. Euclid could measure the Einstein radius with a precision of about 1%, however, we adopt a relative 2% uncertainty to account for additional error contributions from line-of-sight large-scale structures.

3.3 Lensing only results

From the simulated lens catalog described in Section 3.2, we randomly select samples of 100 000 (the “100k” sample) and 400 000 lenses (“400k” sample), from which we evaluate the lensing-only likelihood (Eq. 3.1). We then infer the posterior probability distributions of the parameters v_o , l_o , and b_o using the NAUTILUS sampler [37]. The 1σ and 2σ two-dimensional posterior probability contours for these parameters are shown in Fig. 3. The remaining free parameters, $\langle\theta_E\rangle$ and σ_{θ_E} , are marginalized over and are not shown in this figure. Table 1 summarizes the marginalized posterior constraints obtained both with and without fixing

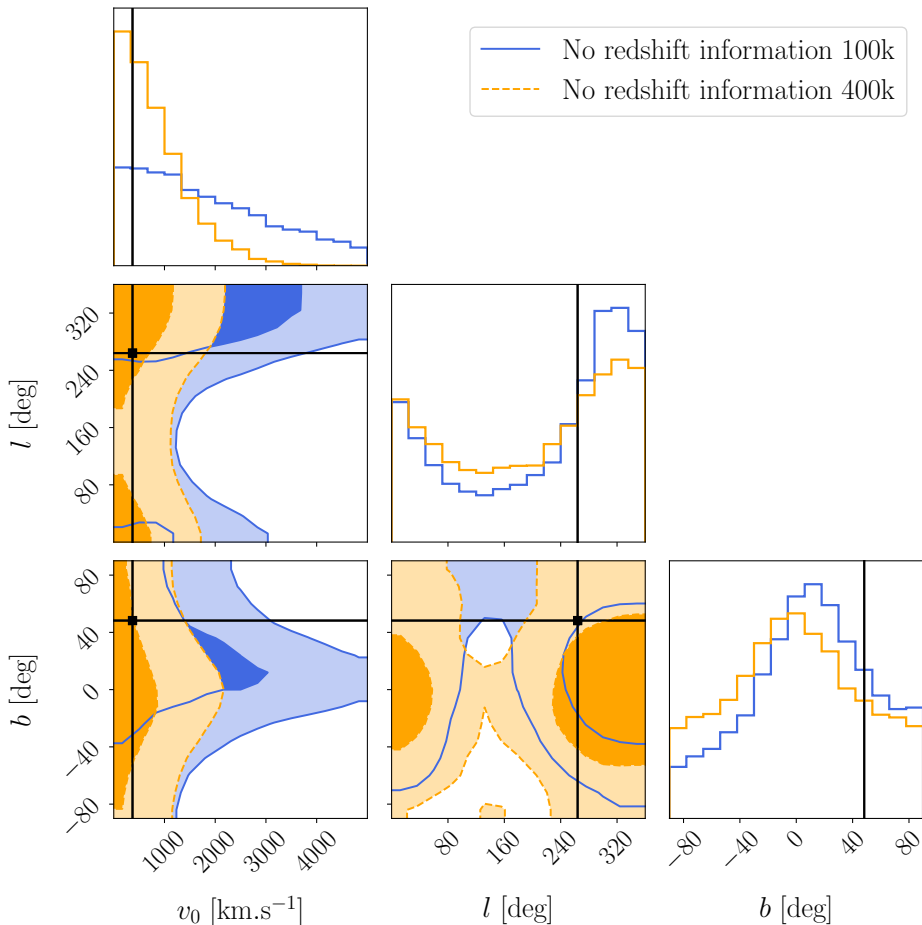


Figure 3. Posterior probability distributions of the kinematic dipole amplitude and direction inferred from samples of 100 000 (blue contours) and 400 000 (orange contours) strong lenses with Euclid-quality imaging. The black lines indicate the true value of $v_o = 369.82 \text{ km s}^{-1}$, pointing toward Galactic coordinates $(l_o, b_o) = (264.021^\circ, 48.253^\circ)$. The contours enclose 39.3% and 86.5% of the posterior probability.

the dipole direction. We repeat the analysis for two different true values of the observer’s peculiar velocity: $v_{o,\text{true}} = 369.82 \text{ km s}^{-1}$, corresponding to the CMB-inferred value, and $v_{o,\text{true}} = 1109.46 \text{ km s}^{-1}$, corresponding to three times the CMB value and consistent with recent results from source number counts [e.g. 11].

While the dipole is detected in both the “100k” and “400k” samples for the highest peculiar velocity, $v_{o,\text{true}} = 1109.46 \text{ km s}^{-1}$, the lowest CMB-inferred value does not produce a sufficiently strong signal to be detected in either sample. Fixing the dipole direction leads to a moderate tightening of the constraints on the dipole amplitude, improving the 68% credible interval width on v_o by approximately 13–16%, depending on the sample size and fiducial velocity.

We therefore find that, when relying on lensing information alone, the Euclid lens sample is unlikely to provide strong discriminatory power between the CMB-inferred dipole amplitude and the larger values suggested by source number count analyzes. The resulting constraints are not sufficiently precise to exclude the CMB-inferred value beyond the $\sim 1.1\sigma$ level, even when fixing the dipole direction and adopting the most optimistic 400 000-lens scenario. We

explore the possibility of including the stellar kinematic information to improve the precision of this measurement in the next section.

Lens sample	$v_{o,\text{true}} = 369.82 \text{ km s}^{-1}$			$v_{o,\text{true}} = 1109.46 \text{ km s}^{-1}$		
	$v_o \text{ [km s}^{-1}\text{]}$	$l \text{ [deg]}$	$b \text{ [deg]}$	$v_o \text{ [km s}^{-1}\text{]}$	$l \text{ [deg]}$	$b \text{ [deg]}$
Lensing only 100k	1608^{+1725}_{-1129}	$263.6^{+64.9}_{-206.3}$	$10.6^{+44.2}_{-45.9}$	1850^{+1741}_{-1254}	$273.0^{+55.6}_{-202.9}$	$20.7^{+42.1}_{-39.8}$
Lensing only 400k	664^{+775}_{-465}	$226.6^{+96.5}_{-175.7}$	$-1.4^{+52.3}_{-49.8}$	844^{+908}_{-597}	$249.8^{+72.7}_{-180.3}$	$23.8^{+41.3}_{-45.7}$
Lensing only 100k - Fixed direction	1618^{+1367}_{-1035}	–	–	2111^{+1376}_{-1251}	–	–
Lensing only 400k - Fixed direction	599^{+610}_{-410}	–	–	1023^{+751}_{-622}	–	–

Table 1. Posterior constraints on the kinematic dipole amplitude and direction using only lensing information. The second and third columns correspond to fiducial values of v_o equal to the CMB-inferred value and three times the CMB value, respectively. The fourth and fifth rows of the table assume a fixed dipole direction toward $(l_o, b_o) = (264.021^\circ, 48.253^\circ)$. Reported values correspond to the 16th, 50th, and 84th percentiles.

4 Combining lensing and Stellar Kinematics

The dominant source of uncertainty in the measurement of the observer velocity arises from the width of the Einstein radius distribution, σ_{θ_E} . This uncertainty can be reduced by incorporating additional information that constrains the unboosted Einstein radius of each ring. We explore two sets of complementary datasets here.

4.1 Spectroscopic velocity dispersion

First, the stellar velocity dispersion of the lens in combination with the source and lens redshifts, provides information about its mass, which directly informs the Einstein radius. More precisely, for a SIS, the central stellar velocity dispersion of the lens galaxy σ_v , relates to the Einstein radius through:

$$\sigma_v = c \sqrt{\frac{\theta_E}{4\pi} \frac{d_s}{d_{l_s}}}, \quad (4.1)$$

where d_s and d_{l_s} are the angular diameter distances between the observer and the source and between the lens and the source, respectively. The dispersion σ_v is measurable from long-slit or fiber spectroscopic observations of the lens galaxy. It is unaffected by the observer’s peculiar velocity because it is a relative measurement of wavelength dispersion. This additional observable provides an estimate of the mass of each lensing galaxy, hence largely reducing the noise term in Eq. (3.1). The fractional measurement error on σ_v translates to θ_E according to:

$$\frac{\delta\sigma_v}{\sigma_v} = \frac{1}{2} \frac{\delta\theta_E}{\theta_E}. \quad (4.2)$$

However, the angular diameter distances d_{l_s} and d_s in Eq. (4.1) have to be inferred from the observed redshifts z'_l , z'_s , and a cosmology, which are biased by the peculiar velocities of the observer, of the lens, and of the source. Using the same notation as in [28], the observed redshifts z'_l , z'_s relate to the cosmological (or background) redshift z_l , z_s in the following way

$$(1 + z_l) = (1 + z'_l) \left(1 + Z_L \frac{v_o}{c} \right), \quad (4.3)$$

$$(1 + z_s) = (1 + z'_s) \left(1 + Z_S \frac{v_o}{c} \right), \quad (4.4)$$

with

$$Z_L = \frac{\hat{\mathbf{n}}' \cdot (\mathbf{v}_o - \mathbf{v}_l)}{v_o}, \quad (4.5)$$

$$Z_S = \frac{\hat{\mathbf{n}}' \cdot (\mathbf{v}_o - \mathbf{v}_s)}{v_o}. \quad (4.6)$$

Propagating these corrections to the background angular diameter distances, one finds, to linear order in v_o/c [28]

$$d_l = d[z'_l] + D_L \frac{v_o}{c}, \quad (4.7)$$

$$d_{ls} = d[z'_l, z'_s] + D_{LS} \frac{v_o}{c}, \quad (4.8)$$

with the distance corrections

$$D_L = \frac{\hat{\mathbf{n}}' \cdot (\mathbf{v}_o - \mathbf{v}_l)}{v_o} \left(\frac{c}{H[z'_l]} - d[z'_l] \right), \quad (4.9)$$

$$D_{LS} = \frac{\hat{\mathbf{n}}' \cdot (\mathbf{v}_o - \mathbf{v}_s)}{v_o} \left(\frac{c}{H[z'_s]} - d[z'_l, z'_s] \right) - \frac{c}{H[z'_l]} \frac{1 + z'_l}{1 + z'_s} \frac{\hat{\mathbf{n}}' \cdot (\mathbf{v}_o - \mathbf{v}_l)}{v_o}. \quad (4.10)$$

Here $H[z] = H_0 E(z) \equiv H_0 \sqrt{\Omega_m(1+z)^3 + (1-\Omega_m)}$ and $\mathbf{v}_l, \mathbf{v}_s$ are the peculiar velocities of the lens and the source galaxy, respectively. Note that Eqs. (4.7) to (4.10) do not represent the observed angular diameter distances of a moving source and lens measured by a boosted observer, since those would also be affected by changes in the area distance, see e.g. [38]. The aim of these expressions is to allow us to find the background angular diameter distances d_l and d_{ls} (that enter in Eq. (4.1)) from the measured redshifts z'_l and z'_s , consistently accounting for the impact of velocities.

The relationship between the observable quantities z'_l, z'_s, σ_v and the predicted Einstein radius $\theta'_{E,\text{spec}}$ is then given by

$$\theta'_{E,\text{spec}} = \frac{4\pi\sigma_v^2}{c^2} \frac{d[z'_l, z'_s]}{d[z'_s]} \left(1 - \frac{v_o}{2c} \cos \theta'_{\text{cm}} + \frac{D_{LS}}{d[z'_l, z'_s]} \frac{v_o}{c} - \frac{D_S}{d[z'_s]} \frac{v_o}{c} \right), \quad (4.11)$$

which can be compared to the observed θ'_E . Contrary to the previous case, our aim here is not to compare each observed ring to the theoretical prediction for the mean $\langle \theta'_E(\hat{\mathbf{n}}') \rangle$ averaged over all source and lens redshifts in a given solid angle. Since we do know the redshifts of the sources and of the lenses, we can improve our analysis by comparing each ring with the theoretical prediction at the correct redshifts, given by Eq. (4.11). In this case, the likelihood becomes:

$$\ln \mathcal{L}_2 = -\frac{1}{2} \sum_{n=1}^N \frac{(\theta'_{E_n} - \theta'_{E_n,\text{spec}} - b_{\text{VD}})^2}{\delta\theta'^2_{E_n} + \delta\theta'^2_{E_n,\text{spec}} + \sigma_{\text{sys,VD}}^2} - \frac{1}{2} \sum_{n=1}^N \ln[2\pi(\delta\theta'^2_{E_n} + \delta\theta'^2_{E_n,\text{spec}} + \sigma_{\text{sys,VD}}^2)], \quad (4.12)$$

where we include a bias and a systematic error term, b_{VD} and $\sigma_{\text{sys,VD}}$, which are fitted as free parameters. When simulating our lens sample, all peculiar velocity terms of the lens, the source, and the observer (Eqs. (4.9) and (4.10)) are included in the simulation. We assume that both the source and lens galaxies have peculiar velocities that are normally distributed, with random orientations and a standard deviation of 300 km s^{-1} . However, at inference, only

the terms involving \mathbf{v}_o can be corrected for (since \mathbf{v}_o also enters into the dipole), while the terms involving \mathbf{v}_l and \mathbf{v}_s are not observable. This source of uncertainty, due to the random peculiar velocities of the lens and the source, is not expected to produce a dipole and is therefore absorbed into the bias and systematic error terms fitted to the data, which also absorb the redshift measurement error, assumed to be $\delta z_{\text{spec}}/z_{\text{spec}} = 0.001$. This error term is small in comparison to the velocity dispersion measurement error.

The uncertainties on the Einstein radius derived from the velocity dispersion measurements, $\theta'_{E_n, \text{spec}}$, are propagated from the uncertainties on σ_v , which we take to be 7%. This translates into a 14% relative uncertainty on $\theta'_{E_n, \text{spec}}$. The 7% uncertainty on σ_v itself combines a 5% contribution from measurement errors, which is conservative compared to the most recent measurement [39, 40] and a 5% contribution from modeling uncertainties, the latter reflecting possible departures of the mass profile from perfect sphericity or isothermality (see Section 5 for a discussion of this issue). The modeling uncertainties could, in theory, be reduced by a more complex axisymmetric Jeans modeling of the lenses instead of the simple SIS assumption, which is sufficient for our forecast.

4.2 Fundamental Plane

Although some spectroscopic follow-up observations of strong lenses are already planned within 4MOST [41], the majority of the Euclid lens sample is unlikely to have spectroscopic velocity-dispersion measurements. Such measurements from ground-based telescopes are expected to be feasible only for the brightest lens galaxies in the sample. However, a larger fraction of the system will have spectroscopic source and lens redshift, or at least, reliable photometric redshifts. An estimation of the central velocity dispersion of the galaxy can be obtained through the Fundamental Plane (FP) relation, which relates the effective radius of the lens R_e , the central velocity dispersion σ_{FP} and the mean surface brightness within the effective radius I_e as

$$\log R_e = a \log \sigma_{\text{FP}} + b \log I_e + c. \quad (4.13)$$

Only the angular size of the effective radius can be directly measured from the imaging data, but R_e can be straightforwardly derived from this measurement and from the (photometric) redshift of the lens, assuming a cosmological model. We assume $a = 1.177$, $b = -0.793$ and $c = 0.5$, obtained from the latest DESI measurement [42]. Measurement errors on these parameters are ignored, as they lead to error much smaller than the intrinsic scatter of the FP. While I_e is invariant under a boost (as shown in the App. D), R_e is not. It can be computed from the observed subtended angle α' and lens redshift z'_l , which are affected by the boost, as

$$R_e = \alpha d_l = \alpha' d[z'_l] \left(1 + \frac{v_o}{2c} \cos(\theta'_{\text{cm}}) + \frac{D_L}{d[z'_l]} \frac{v_o}{c} \right). \quad (4.14)$$

As a result, the velocity dispersion σ_{FP} determined from the FP is also affected by the peculiar velocities, as discussed in detail in App. D. On average, the observed Einstein angle θ'_{E} can be expressed as

$$\theta'_{E, \text{FP}} = \frac{4\pi\sigma_{\text{FP}}^2}{c^2} \frac{d[z'_l, z'_s]}{d[z'_s]} \left(1 - \frac{1}{2} \frac{v_o}{c} \cos(\theta'_{\text{cm}}) + \frac{D_{LS}}{d[z'_l, z'_s]} \frac{v_o}{c} - \frac{D_S}{d[z'_s]} \frac{v_o}{c} + 2\Sigma_v \frac{v_o}{c} \right), \quad (4.15)$$

where σ'_{FP} and Σ_v are defined as

$$\sigma'_{\text{FP}} = \left(10^{-c} \alpha' d[z'_l] (I_e)^{-b} \right)^{1/a}, \quad (4.16)$$

$$\Sigma_v = \left(\frac{1}{2a} \cos(\theta'_{\text{cm}}) + \frac{D_L}{ad[z'_l]} \right). \quad (4.17)$$

Eq. (4.15) can be used to infer v_o from the observables $\theta'_E, z'_l, z'_s, \alpha', I'_e, \theta'_{\text{cm}}$ and the parameters a, b, c . In practice, it is, however, more convenient to define the likelihood in terms of the velocity dispersion rather than the Einstein radius, i.e., to compare σ'_{FP} with the velocity dispersion σ'_{SIS} inferred from θ'_E using Eq. (4.1). σ'_{FP} indeed has a large scatter, which is squared in Eq. (4.15), breaking down the assumption of a Gaussian likelihood. The likelihood function is hence defined as:

$$\ln \mathcal{L}_3 = -\frac{1}{2} \sum_{n=1}^N \frac{(\sigma'_{\text{SIS},n} - \sigma'_{\text{FP},n} - b_{\text{FP}})^2}{\delta\sigma_{\text{SIS},n}^2 + \delta\sigma_{\text{FP},n}^2 + \sigma_{\text{sys,FP}}^2} - \frac{1}{2} \sum_{n=1}^N \ln \left[2\pi (\delta\sigma_{\text{SIS},n}^2 + \delta\sigma_{\text{FP},n}^2 + \sigma_{\text{sys,FP}}^2) \right]. \quad (4.18)$$

Details on how the uncertainties $\delta\sigma_{\text{FP}}$ are calculated can be found in App. C. Similarly to Eq. (4.12), we introduced a bias and systematic error term to account for model mismatch, peculiar velocity effects, and redshift measurement errors when converting Einstein angles to velocity dispersions. We treat separately the likelihood contributions from lenses with only photometric redshift estimates and those with spectroscopic redshift measurements for both source and lens, since these two subsamples require different bias and systematic error corrections owing to the differing precision of their redshift determinations.

All variables used in the simulation are listed in Table 2.

4.3 Euclid Forecast

We illustrate the gain in constraining power obtained by adding velocity-dispersion information for the “100k” lens sample, relative to the lensing-only case, in Figure 4. When only photometric redshift estimates for the lenses and sources are available, and the velocity dispersion is inferred using FP relations, the precision on v_o improves by a factor of ~ 1.5 . If spectroscopic redshift measurements for both the lens and the source are available, the constraints improve by a factor of ~ 3 compared to the lensing-only case. In the perfect scenario in which all lenses have spectroscopic redshifts for both the lens and the source, as well as direct spectroscopic measurements of the stellar velocity dispersion, the constraint improves by a factor of ~ 10 . In the latter case, the inferred precision becomes sufficient to discriminate between the CMB-inferred value and the value suggested by the source number count analyzes at $5.6 - 5.8\sigma$ (depending on the fiducial value assumed for v_o). All posterior distributions are reported in Table 4 as well as the exclusion significance of the alternative value of v_o , averaged over five different realizations of the lens sample.

Finally, we assess the constraining power of several spectroscopic follow-up scenarios for the Euclid strong-lens sample. In a first, *pessimistic* scenario, we assume that only 15 000 lenses receive spectroscopic follow-up, either from large spectroscopic surveys such as DESI [45] or 4MOST [41, 46], or from dedicated follow-up programs. While both redshift and stellar velocity-dispersion measurements are in principle accessible with fiber spectroscopy, the latter are significantly more challenging, as they require a higher signal-to-noise ratio to robustly detect the absorption features of the lens galaxy. As a result, even if a lens is targeted by DESI or 4MOST, a substantial fraction of systems are expected to yield redshift measurements only. In this pessimistic scenario, we therefore assume that velocity-dispersion

Simulation	Value	Description
$\delta\theta'_E/\theta'_E$	2%	Measurement error on θ'_E from the Euclid images
$\delta\sigma_v/\sigma_v$	7%	Relative error on the spectroscopic measurement of σ_v , Ref. [39, 40]
$\delta z_{\text{spectro}}/z_{\text{spectro}}$	0.001	Spectroscopic redshift measurement error, Ref. [43]
$\delta z_{\text{photo}}/z_{\text{photo}}$	0.03	Photometric redshift measurement error, Ref. [43]
v_{pec}	300 km s^{-1}	Standard deviation of the peculiar velocity galaxies
a	1.177	FP coefficient (Eq. 4.13), Ref. [42]
b	-0.793	FP coefficient (Eq. 4.13), Ref. [42]
c	-0.206	FP coefficient (Eq. 4.13), Ref. [42]
σ_1	0.059	Scatter perpendicular to the FP (Eq. C.6), Ref. [42]
σ_2	0.392	Scatter along the FP (long axis, Eq. C.6), Ref. [42]
σ_3	0.256	Scatter along the FP (short axis, Eq. C.6), Ref. [42]
\bar{s}	2.102	Mean s of the FP (Eq. C.3), Ref. [42]
\bar{i}	2.653	Mean i of the FP (Eq. C.3), Ref. [42]
\bar{r}	0.165	Mean r of the FP (Eq. C.3), Ref. [42]
ϵ_r	0.041 dex	Measurement error on r (Eq. C.10), [44]
ϵ_i	0.060 dex	Measurement error on i (Eq. C.10), [44]
Inference	Prior	
$ v_o $	$\mathcal{U} \sim (0, 5000) \text{ km s}^{-1}$	Velocity of the observer
l_o	$\mathcal{U} \sim (0, 360) \text{ deg}$	Direction of the observer's velocity in galactic coordinates
b_o	$\mathcal{U} \sim (-90, 90) \text{ deg}$	Direction of the observer's velocity in galactic coordinates
θ_E	$\mathcal{U} \sim (0, 2)''$	Mean Einstein radius of the sample
σ_{θ_E}	$\mathcal{U} \sim (0, 1)''$	Standard deviation of the Einstein radius distribution
b_{VD}	$\mathcal{U} \sim (-1, 1)''$	Bias in spectroscopic determination of $\langle\theta'_E\rangle_{\text{spec}}$
$b_{\text{FP-spectro}}$	$\mathcal{U} \sim (-300, 300) \text{ km s}^{-1}$	Bias in FP determination of σ_{FP} (spectroscopic redshifts)
$b_{\text{FP-photo}}$	$\mathcal{U} \sim (-300, 300) \text{ km s}^{-1}$	Bias in FP determination of σ_{FP} (photometric redshifts)
$\sigma_{\text{sys, VD}}$	$\mathcal{U} \sim (0, 1)''$	Systematic error in $\langle\theta'_E\rangle_{\text{spec}}$
$\sigma_{\text{sys, FP-spectro}}$	$\mathcal{U} \sim (0, 300) \text{ km s}^{-1}$	Systematic error σ_{FP} (spectroscopic redshifts)
$\sigma_{\text{sys, FP-photo}}$	$\mathcal{U} \sim (0, 300) \text{ km s}^{-1}$	Systematic error σ_{FP} (photometric redshifts)

Table 2. List of variables used in the simulation of the lens sample and observables, together with the priors adopted for the inference.

measurements are successfully obtained for only a third of the spectroscopically targeted lenses, i.e. 5 000 lenses. The remaining lenses are assumed to have spectroscopic, photometric, or no redshift information, as summarized in Table 3.

In a more *realistic* scenario, we assume that the majority of lenses benefit from at least partial redshift information, either from follow-up spectroscopic observations, Euclid NISP slitless spectroscopy, or, at minimum, reliable photometric redshift estimates. In this case, we adopt a similar success rate for velocity-dispersion measurements, yielding 10 000 lenses with kinematic information out of 30 000 targeted lenses.

The third, *ideal* scenario corresponds to a dedicated spectroscopic survey of strong lenses, in which all lenses are followed up. We assume a velocity-dispersion measurement success rate of 50%, resulting in 50 000 lenses with stellar velocity-dispersion measurements and an additional 50 000 lenses with spectroscopic redshifts for both the lens and the source.

We show the posterior distribution contours for the three scenarios in Figure 5, assuming a fiducial peculiar velocity $v_{o,\text{true}} = 1109.46 \text{ km s}^{-1}$. The median values, together with the 16th and 84th percentiles of the marginalized posterior distributions, are reported in Table 4 for a single realization of the lens samples. In addition, we quote the significance at which the alternative value of v_o is excluded, averaged over five independent realizations for each scenario.

For a fiducial value of $v_{o,\text{true}} = 1109.46 \text{ km s}^{-1}$, all three spectroscopic follow-up scenarios exclude the CMB-inferred value of v_o with a significance ranging from 1.7σ in the pessimistic

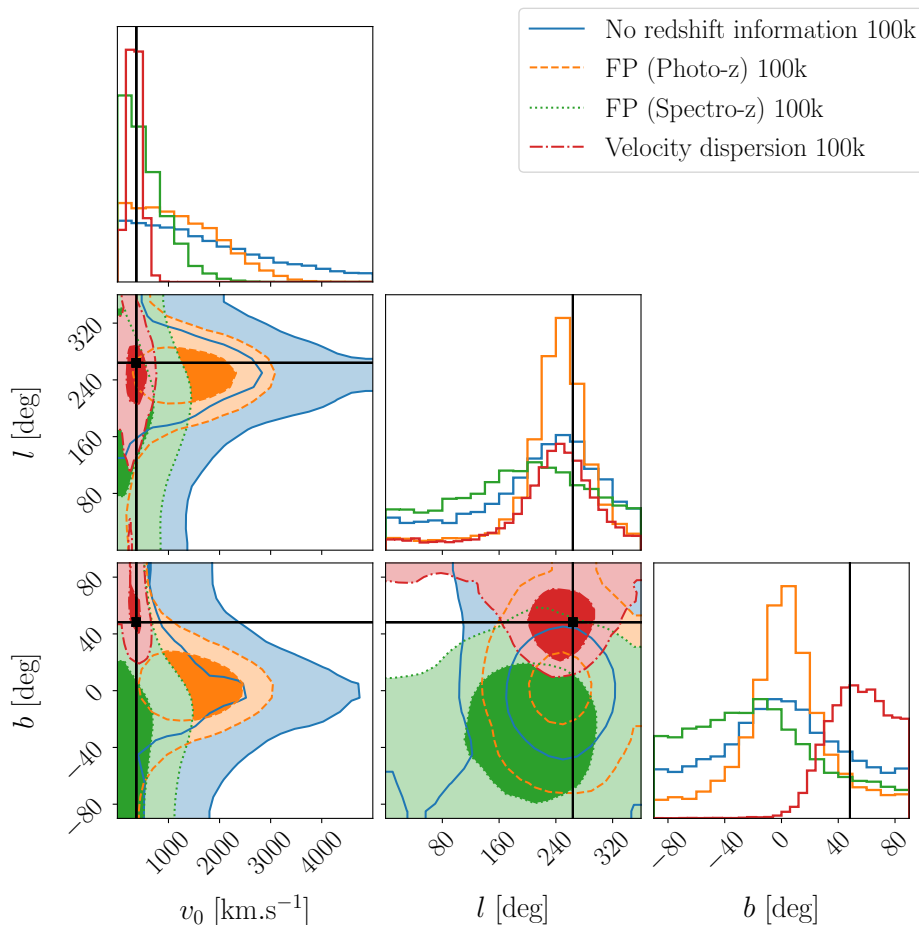


Figure 4. Posterior probability distributions of the kinematic dipole amplitude and direction inferred from samples of 100 000 strong lenses with Euclid-quality imaging (blue contours), in combination with spectroscopic stellar velocity dispersion measurements (red contours), or with FP estimates of the velocity dispersion using spectroscopic redshifts (green contours) or photometric redshifts (orange contours). The black lines indicate the true value of $v_o = 369.82 \text{ km s}^{-1}$, pointing towards Galactic coordinates $(l_o, b_o) = (264.021^\circ, 48.253^\circ)$. The contours enclose 39.3% and 86.5% of the posterior probability.

	Scenario 1 (Pessimistic)	Scenario 2 (Realistic)	Scenario 3 (Ideal)
No photo- z	35 000	-	-
FP with photo- z	50 000	70 000	-
FP with spec- z	10 000	20 000	50 000
With vel. disp.	5 000	10 000	50 000
Total	100 000	100 000	100 000

Table 3. Number of lenses with available ancillary information for Euclid pessimistic, realistic and ideal scenarios.

scenario to 4.1σ in the ideal scenario. Conversely, when the CMB-inferred value of v_o is adopted as the fiducial velocity, the source number-count value is excluded with a significance ranging from 1.3σ to 4.2σ across the same scenarios. These results indicate that strong-lensing

Lens sample	$v_{o,\text{true}} = 369.82 \text{ km s}^{-1}$			$v_{o,\text{true}} = 1109.46 \text{ km s}^{-1}$		
	$v_o \text{ [km.s}^{-1}\text{]}$	$l \text{ [deg]}$	$b \text{ [deg]}$	$v_o \text{ [km.s}^{-1}\text{]}$	$l \text{ [deg]}$	$b \text{ [deg]}$
Lensing only 100k	$1436^{+1638}_{-1011} (0.5\sigma)$	$228.4^{+69.1}_{-115.4}$	$-0.3^{+49.0}_{-48.6}$	$1629^{+1718}_{-1148} (0.7\sigma)$	$233.6^{+62.5}_{-108.6}$	$11.2^{+43.9}_{-46.7}$
FP (Photo-z) 100k	$1090^{+959}_{-758} (1.1\sigma)$	$243.7^{+36.9}_{-46.9}$	$2.5^{+28.1}_{-27.3}$	$1713^{+895}_{-971} (1.0\sigma)$	$259.5^{+26.4}_{-29.3}$	$7.4^{+19.7}_{-16.7}$
FP (Spectro-z) 100k	$463^{+521}_{-327} (1.2\sigma)$	$196.2^{+93.1}_{-111.1}$	$-19.2^{+51.1}_{-45.3}$	$954^{+596}_{-546} (1.2\sigma)$	$103.2^{+191.0}_{-67.4}$	$49.2^{+26.9}_{-31.3}$
Velocity dispersion 100k	$339^{+135}_{-127} (5.8\sigma)$	$240.9^{+47.9}_{-68.7}$	$54.5^{+22.7}_{-22.3}$	$1111^{+140}_{-135} (5.6\sigma)$	$258.0^{+13.5}_{-13.2}$	$48.8^{+8.1}_{-7.1}$
Scenario 1 (Pessimistic)	$636^{+431}_{-388} (1.3\sigma)$	$208.6^{+92.4}_{-130.1}$	$53.1^{+25.2}_{-34.8}$	$1011^{+436}_{-416} (1.7\sigma)$	$256.9^{+68.4}_{-192.0}$	$60.2^{+20.4}_{-24.3}$
Scenario 2 (Realistic)	$715^{+394}_{-356} (1.7\sigma)$	$214.4^{+51.7}_{-61.2}$	$44.1^{+28.5}_{-25.3}$	$1436^{+426}_{-422} (2.2\sigma)$	$262.8^{+22.9}_{-20.8}$	$36.3^{+17.5}_{-12.5}$
Scenario 3 (Ideal)	$541^{+157}_{-156} (4.2\sigma)$	$237.5^{+67.9}_{-132.1}$	$69.4^{+14.1}_{-19.1}$	$1272^{+174}_{-176} (4.1\sigma)$	$257.8^{+20.8}_{-20.3}$	$57.4^{+10.9}_{-9.2}$

Table 4. Posterior constraints on the kinematic dipole amplitude and direction using either lensing-only or combined lensing+kinematic information, obtained from direct spectroscopic measurements or from FP estimates. Scenarios 1 and 2 correspond to plausible ancillary information expected to be available for the Euclid lens sample (see Table 3). The second and third columns correspond to fiducial values of v_o equal to the CMB-inferred value and three times the CMB value, respectively. Reported values correspond to the 16th, 50th, and 84th percentiles. Values in parentheses indicate the one-sided Gaussian-equivalent significance at which the alternative fiducial value of v_o is excluded, averaged over 5 realizations of the lens sample.

measurements could provide valuable complementary information on the cosmic dipole tension in realistic spectroscopic follow-up configurations, with a potential discrimination between the two values of v_o at the $\sim 2\sigma$ level. In the presence of a dedicated spectroscopic follow-up of strong lenses, however, this probe could make a decisive contribution to this debate, with a discriminating power exceeding 4σ .

5 Discussion

As shown in the previous section, strong-lensing measurements can reach a sufficient level of precision to discriminate between the CMB-inferred and source number-count values of v_o , provided that adequate spectroscopic follow-up data are available for a large fraction of the Euclid strong-lens sample. This method would offer an independent test of the cosmic dipole, with systematic uncertainties that are fundamentally different from those affecting source number-count measurements.

Systematic errors: A primary advantage of this method is that any bias in the absolute calibration of the FP, the measurement of the velocity dispersion, or the dynamical modeling of the galaxies (assumed to be an SIS in this paper) becomes irrelevant, provided such biases are uniform across the sky. However, the observer’s peculiar velocity directly modulates the FP observable R_e through two distinct relativistic effects. First, R_e is subject to angular aberration, analogous to that observed in the Einstein angle (Eq. (2.13)). Second, the observer’s peculiar velocity affects the conversion of the angular scale α of the galaxy into a physical scale R_e (in kpc) via the angular diameter distance, since the estimated redshift of the galaxy is impacted by the observer’s motion. Both effects are explicitly accounted for in the expression of the likelihood (Eq. (4.18)), ensuring that the inferred v_o is unbiased.

Since the monopole and dipole are fitted simultaneously, extensive sky coverage is necessary to prevent biases in the inferred dipole amplitude. This is especially true for the lensing-only measurement (Sec. 3), as the Einstein angle is not compared against any absolute calibration, leading to a potential degeneracy between the monopole and dipole amplitudes if the sky coverage is insufficient. This effect can originate, for example, from galaxy clustering,

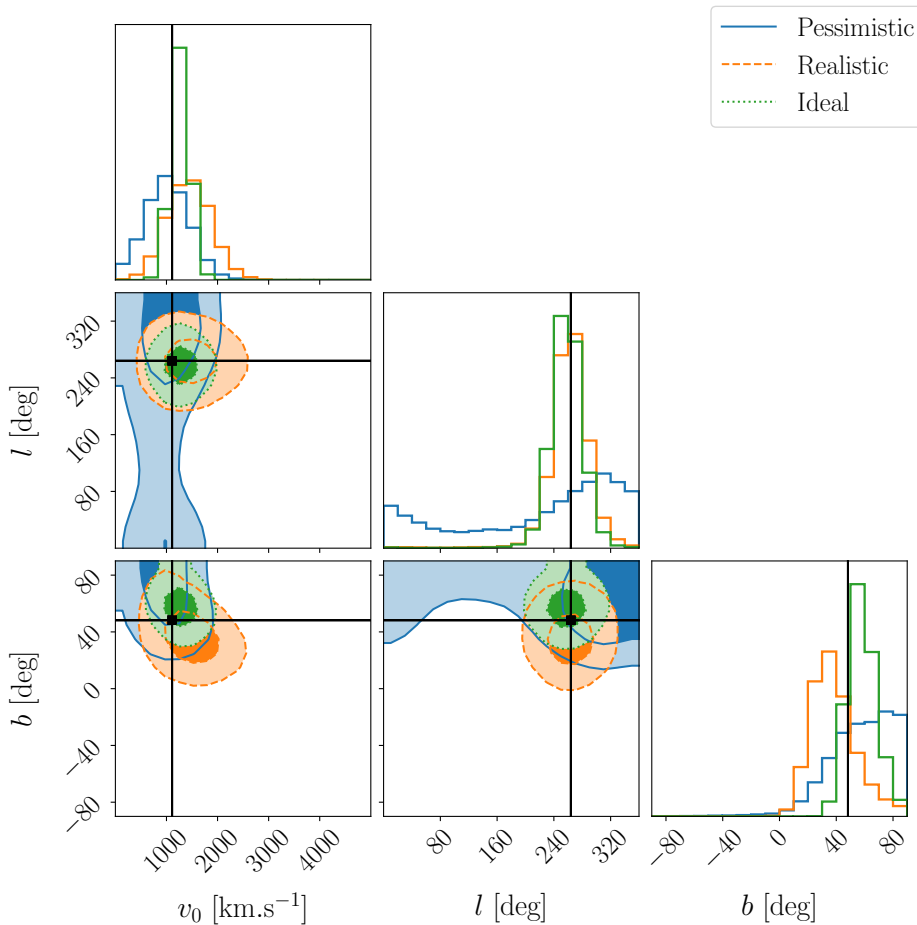


Figure 5. Posterior probability distributions of the kinematic dipole amplitude and direction inferred from samples of 100 000 strong lenses with Euclid-quality imaging and different type of ancillary kinematic information, listed in Table 3. The black lines indicate the true value of $v_o = 1109.42 \text{ km s}^{-1}$, pointing towards Galactic coordinates $(l_o, b_o) = (264.021^\circ, 48.253^\circ)$. The contours enclose 39.3% and 86.5% of the posterior probability.

which can modify both the average Einstein radius of the lenses and their number density on small scales, since denser regions of the Universe are expected to have a higher probability of lensing [47] and to produce larger Einstein radii. The area covered by the Euclid Wide Survey, which spans approximately 14 000 square degrees across both hemispheres, should, however, be largely sufficient to break this degeneracy.

Strong lensing selection function: One of the main challenges in analyzing large samples of strong lenses is the characterization of the selection function, which can be particularly complex due to the diversity of lens-search algorithms used to identify the systems [48–50]. In Appendix B, we explicitly calculate the impact of the selection function on the dipole, for the lensing only probe. As we will see, the contribution is extremely small, less than 0.1%, meaning that it is not necessary to model the selection function to infer the observer’s velocity. We consider two selections, the first one on the (magnified) flux of the source, and the second

one on the size of the Einstein ring, such that the mean radius is given by

$$\begin{aligned} \langle \theta'_E(\hat{\mathbf{n}}') \rangle &= \left(\frac{dN(\hat{\mathbf{n}}', \theta'_E > \theta'_{E*}, F' > F'_*)}{d\Omega'} \right)^{-1} \\ &\times \int dz'_s \int dz'_l \int_{\theta'_{E*}} d\theta'_E \frac{dN(\hat{\mathbf{n}}', z'_s, z'_l, \theta'_E, F' > F'_*)}{d\Omega' dz'_s dz'_l d\theta'_E} \theta'_E(\hat{\mathbf{n}}', z'_s, z'_l), \end{aligned} \quad (5.1)$$

where F'_* is the observed flux threshold of the source and θ'_{E*} is the observed size threshold. These selection effects have the potential to modulate the mean Einstein radius of the sample $\langle \theta'_E \rangle$ in the dipole direction, leading to a bias in v_o if not properly accounted for. In the presence of kinematic data, however, the Einstein radii are compared on a per-lens basis, and therefore these selection effects, which affect the sample mean, become irrelevant.

Here, we consider hard cuts in flux and Einstein radius, but a smoother selection function would lead to even smaller biases. The flux threshold contributes to the dipole because a fixed observer-frame flux limit, F'_* , translates into a direction-dependent threshold in the intrinsic luminosity, $L_*(\hat{\mathbf{n}}', z'_s)$. This arises because the luminosity distance—which relates the observed flux to the intrinsic luminosity—is itself affected by the boost. As a consequence, the moving observer does not see the same number of rings in the direction of the boost as in the opposite direction. The same argument applies to the size threshold: a fixed threshold in the observer frame corresponds to different intrinsic sizes of the rings in different directions.

The detailed calculation can be found in Appendix B, where we found²

$$\begin{aligned} \langle \theta'_E \rangle &= \langle \theta_E \rangle \left(1 - \frac{v_o}{2c} \cos \theta'_{\text{cm}} \right) \\ &+ 2 \frac{v_o}{c} \cos \theta'_{\text{cm}} \int dz'_s \int_{\theta'_{E*}} d\theta'_E (\theta'_E - \langle \theta_E \rangle) f_1(z'_s, \theta'_E, F' > F'_*) x(z'_s, \theta'_E, F'_*) \\ &+ \frac{v_o}{2c} \cos \theta'_{\text{cm}} (\langle \theta_E \rangle - \theta'_{E*}) \int dz'_s \int dz'_l f_2(z'_s, z'_l, \theta'_{E*}, F' > F'_*) \mu(z'_s, z'_l, \theta'_{E*}, F'_*). \end{aligned} \quad (5.2)$$

Here f_1 is the distribution of detected rings (integrated over the redshift of the lenses) as a function of θ'_E ; and f_2 is the cumulative distribution above the size threshold, see Eqs. (B.16) and (B.17). The relativistic magnification bias x and the parameter μ govern the amplitude of the threshold effects and are given by

$$x(z'_s, \theta'_E, F'_*) = - \frac{\partial \ln}{\partial \ln F'_*} \left(\frac{dN(z'_s, \theta'_E, F' > F'_*)}{d\Omega dz'_s d\theta'_E} \right), \quad (5.3)$$

$$\mu(z'_s, z'_l, \theta'_{E*}, L_*) = - \frac{\partial \ln}{\partial \ln \theta'_{E*}} \left(\frac{dN(z'_s, z'_l, \theta'_E > \theta'_{E*}, F' > F'_*)}{d\Omega dz'_s dz'_l} \right). \quad (5.4)$$

They represent the slope of the cumulative distribution of rings above the respective thresholds and therefore quantify how many more systems we detect in one direction because the flux and the size are boosted. For a complete sample, x and μ vanish exactly. In practice, these parameters can be estimated from the population of rings by binning the systems in flux and size, and measuring the slopes at different thresholds.

What is interesting from Eq. (5.2) is that the selection effects are strongly suppressed with respect to the case where we simply count objects. This is due to the fact that the

²As shown in the Appendix B, all functions are written in principle in terms of unboosted quantities. However, at the lowest order in v_o/c , we can replace the unboosted quantities (a priori unknown) with the boosted ones, such that functions are expressed in terms of observable quantities.

mean $\langle\theta'_E\rangle$ is normalized by the number of detected rings. The modulation in the number of rings induced by threshold effects impacts both the numerator and the denominator in Eq. (5.1), and the two contributions partially cancel out, leading to a negligible impact. For example, the second term in Eq. (5.2), representing the effect of the selection in flux, is strongly suppressed by the $(\theta'_E - \langle\theta_E\rangle)$ term. If the parameter $x(z'_s, \theta'_E, F'_*)$ was independent of z'_s and θ'_E , then this contribution would be exactly zero since it would not change the sample mean $\langle\theta_E\rangle$. In practice, this is not the case, since the observed source flux is related to z'_s and θ'_E through the lensing magnification. However, this means that the surviving contribution is proportional to the change in the mean sample induced by the flux selection. We have computed this effect by evaluating x from our sample and computing the second line of Eq. (5.2), and we have found that it generates a negligible contribution to the dipole that is $< 10^{-6}$ of the main effect.

The contribution from the size threshold, encoded in the third line of Eq. (5.2), is also suppressed, but this time by a factor $(\langle\theta_E\rangle - \theta'_{E*})$. In this case, there is a balance between this factor and the parameter μ . If most systems have sizes well above the threshold θ'_{E*} , then $(\langle\theta_E\rangle - \theta'_{E*})$ will be large, but the effect will be strongly suppressed by μ , which tends to zero in the limit where there are no rings below the threshold. Conversely, if most rings lie close to the threshold, then μ can be large, but the effect is suppressed by $(\langle\theta_E\rangle - \theta'_{E*})$, which becomes small for rings near the threshold. We estimate the magnitude of this effect by evaluating μ from our sample, assuming a threshold of $\theta'_{E*} = 0.2''$, and computing the third line of Eq. (5.2). We find that this contribution is of order 0.05% of the main effect. Although significantly larger than the contribution from the flux threshold, it remains completely negligible compared to the main effect.

This demonstrates that the dipole in the Einstein rings is almost insensitive to the strong lensing selection function, provided it is uniform across the sky. As such, it provides a very robust way of measuring the observer velocity. In other words, neglecting these threshold effects would bias the measurement of the observer velocity by 0.05% at most, largely below the statistical uncertainty.

Limitations of the model: In this study, we developed a simple Bayesian framework to assess whether a dipolar modulation of the Einstein angle induced by the observer’s peculiar velocity can be measured from future, yet realistic, samples of strong lenses. Although our lens population model accounts for the selection function of the lenses, we assumed simple Gaussian probability distributions for the measurements of the Einstein angle, stellar velocity dispersion, and redshifts, as well as a trivariate Gaussian model for the FP. However, when propagating these uncertainties through the likelihood (Eq. (4.18)), the Gaussian approximation proved insufficient. To address this limitation, we introduced a bias term and an additional systematic error term, which were sufficient to capture the leading-order deviations from Gaussianity and to recover unbiased measurements of v_o , l_o , and b_o . A full hierarchical Bayesian inference framework will be required to model these effects more rigorously. Such an approach would allow the measurement uncertainties and intrinsic scatter of the lens and source populations to be modeled consistently at the population level, rather than being absorbed into effective bias and systematic error terms. This may further improve the precision and robustness of the dipole measurement. We leave such an analysis for future work.

Finally, a main limitation of this study is that we ignore the impact of ellipticity in the mass distribution of the lensing galaxies and cosmic shear. The ellipticity of the Einstein ring contains additional directional information that could help constrain the dipole direction while

simultaneously acting as a source of noise when combining lensing and kinematic information. In the lensing-only case, we emphasize that we use the *azimuthally averaged* Einstein radius as our primary observable. This quantity is sensitive to the enclosed mass of the galaxy, the angular-diameter–distance ratio, and cosmic convergence, which is expected to average out on large scales. In the lensing+kinematic case, ellipticity in the mass distribution of the lens galaxy introduces additional scatter in the predicted central velocity dispersion. Departures from isothermality in the mass profile would produce a similar effect. In this work, we account for both sources of uncertainty by adopting a 5% modeling error in addition to the 5% measurement error. Future improvements of this technique may include full dynamical modeling of the lenses as well as shear and convergence correction from weak lensing maps, allowing one to exploit the directional information encoded in the elliptical deformation of the Einstein ring. The aberration due to the observer’s velocity might appear as a dipole component in the line-of-sight shear of strong gravitational lenses, proposed by [51].

6 Conclusion

In this work, we present a novel method that could provide a fully-independent way of measuring the kinematic cosmic dipole, based on angle measurement rather than the traditional number counts technique, which relies on flux measurements. Our main findings are the following:

- A detection of the dipolar modulation of the Einstein radii of strong lenses is possible using the lensing information contained in Euclid images alone, but only in the case where the velocity is as large as inferred from the number-count analyses.
- The inclusion of kinematic information, either through spectroscopic velocity-dispersion measurements or via FP relations, significantly improves the constraining power of the method. Even in the absence of spectroscopic redshift information, the combination of FP relations and photometric redshifts leads to an improvement of $\sim 50\%$ compared to lensing-only constraints.
- Already existing or planned spectroscopic follow-up observations from 4MOST [41] and DESI [e.g., 52] should yield a discriminating power at the level of $\sim 2\sigma$ between the value of v_o measured from the CMB and that measured from sources number counts.
- A hypothetical dedicated strong-lensing spectroscopic follow-up of the full Euclid sample could provide a decisive contribution to this debate, with a discriminating power reaching $\sim 4\sigma$.
- The method is mostly insensitive to the lens selection function, provided it is spatially uniform over the survey footprint. Similarly, any bias in the lens mass modeling or in the dynamical modeling of the lenses can be self-calibrated from the data and does not affect the measurement of v_o , as long as these biases are constant across the sky.

The recent discovery of hundreds of new strong-lens systems in the Euclid Q1 data highlights the potential to increase the current sample of known lenses by two orders of magnitude with the full Euclid survey. With such a large sample, we propose a direct cosmological test that can be performed using the imaging survey data, complemented by modest spectroscopic follow-up from Euclid NISP, DESI, or 4MOST.

Acknowledgments

MM acknowledges support from the Swiss National Science Foundation (SNSF) through return CH grant P5R5PT.225598 and Ambizione grant PZ00P2.223738. This work has received funding from the European Research Council (ERC) under the European Union's Horizon 2020 research and innovation program (LensEra: grant agreement No 945536). TEC is funded by the Royal Society through a University Research Fellowship. CB acknowledges support from the Swiss National Science Foundation (SNSF).

A Calculation of the mean Einstein radius integrated over redshifts

To calculate Eq. (2.9), we need to compute the Einstein angle and the number of sources as functions of the measured redshifts z'_s and z'_l . These redshifts are affected by the observer velocity v_o through

$$1 + z'_s = (1 + z_s) \left(1 - \frac{v_o}{c} \cos \theta'_{\text{cm}} \right), \quad (\text{A.1})$$

$$1 + z'_l = (1 + z_l) \left(1 - \frac{v_o}{c} \cos \theta'_{\text{cm}} \right). \quad (\text{A.2})$$

The component of θ'_E along the \mathbf{e}'_1 direction at fixed z'_s and z'_l is given by

$$\theta'_{E1}(\delta', \hat{\mathbf{n}}', z'_s, z'_l) = \theta'_{E1}(\delta', \hat{\mathbf{n}}', r'(z'_s, \hat{\mathbf{n}}'), r'(z'_l, \hat{\mathbf{n}}')), \quad (\text{A.3})$$

where $r'(z'_s, \hat{\mathbf{n}}')$ is the comoving distance associated with the boosted redshift z'_s , which depends on direction $\hat{\mathbf{n}}'$ through the impact of the boost on the redshift. We split this distance into an isotropic part and a perturbation

$$r'(z'_s, \hat{\mathbf{n}}') = r(z'_s) + \delta r(z'_s, \hat{\mathbf{n}}'). \quad (\text{A.4})$$

As shown in [13], the perturbation in the distance is given by

$$\delta r(z'_s, \hat{\mathbf{n}}') = \frac{1}{\mathcal{H}(z'_s)} \frac{v_o}{c} \cos \theta'_{\text{cm}}. \quad (\text{A.5})$$

Doing the same split for the redshift of the lens, we can insert them into (A.3) and Taylor expand at linear order in v_o/c

$$\theta'_{E1}(\delta', \hat{\mathbf{n}}', z'_s, z'_l) = \theta_E(\delta', r(z'_s), r(z'_l)) \cos \delta' + \left(\frac{\partial \theta_E}{\partial r_s \mathcal{H}(z'_s)} + \frac{\partial \theta_E}{\partial r_l \mathcal{H}(z'_l)} \right) \cos \delta' \frac{v_o}{c} \cos \theta'_{\text{cm}}. \quad (\text{A.6})$$

From this we see that even though the angles along \mathbf{e}'_1 are not aberrated, the fact that the redshifts of the lens and of the source are affected by the boost has an impact on θ'_{E1} . Physically, this is due to the fact that a source at fixed redshift z'_s is not at the same physical distance from the observer if it is in the direction of the boost or if it is in the opposite direction. Since the Einstein radius depends on the distance of the source, this impacts the observed θ'_{E1} . The calculation for θ'_{E2} is similar, with the effect from the redshift added to the effect of aberration

$$\theta'_{E2}(\delta', \hat{\mathbf{n}}', z'_s, z'_l) = \theta_E(\delta', r(z'_s), r(z'_l)) \sin \delta' \left(1 - \frac{v_o}{c} \cos \theta'_{\text{cm}} \right) \quad (\text{A.7})$$

$$+ \left(\frac{\partial \theta_E}{\partial r_s \mathcal{H}(z'_s)} + \frac{\partial \theta_E}{\partial r_l \mathcal{H}(z'_l)} \right) \sin \delta' \frac{v_o}{c} \cos \theta'_{\text{cm}}.$$

Computing $\theta'_E(\delta', \hat{\mathbf{n}}', z'_s, z'_l)$ and averaging over δ' , we find

$$\theta'_E(\hat{\mathbf{n}}', z'_s, z'_l) = \theta_E(r(z'_s), r(z'_l)) \left(1 - \frac{v_o}{2c} \cos \theta'_{\text{cm}} \right) + \left((1+z_s) \frac{\partial \theta_E}{\partial z_s} + (1+z_l) \frac{\partial \theta_E}{\partial z_l} \right) \frac{v_o}{c} \cos \theta'_{\text{cm}}, \quad (\text{A.8})$$

where we have used that $\partial/\partial r = \mathcal{H}(1+z)\partial/\partial z$.

To obtain the mean Einstein radius in a solid angle $d\Omega'$, we need to weight it by the number of systems at fixed z'_s, z'_l . We have

$$\begin{aligned} \frac{dN(z'_s, z'_l, \hat{\mathbf{n}}')}{d\Omega' dz'_s dz'_l} &= \frac{dN(r(z'_s), r(z'_l))}{d\Omega dz_s dz_l} \left(1 - \frac{\delta\Omega}{\Omega} - \frac{\delta z_s}{1+z_s} - \frac{\delta z_l}{1+z_l} \right) \\ &+ \frac{\partial}{\partial r_s} \left(\frac{dN}{d\Omega dz_s dz_l} \right) \delta r_s + \frac{\partial}{\partial r_l} \left(\frac{dN}{d\Omega dz_s dz_l} \right) \delta r_l \\ &= \frac{dN(r(z'_s), r(z'_l))}{d\Omega dz_s dz_l} \left(1 + 4 \frac{v_o}{c} \cos \theta'_{\text{cm}} \right) \\ &+ \left[(1+z_s) \frac{\partial}{\partial z_s} \left(\frac{dN}{d\Omega dz_s dz_l} \right) + (1+z_l) \frac{\partial}{\partial z_l} \left(\frac{dN}{d\Omega dz_s dz_l} \right) \right] \frac{v_o}{c} \cos \theta'_{\text{cm}}. \end{aligned} \quad (\text{A.9})$$

Multiplying Eq. (A.9) with (A.8) and using that

$$\frac{\partial}{\partial z_s} \left(\frac{dN}{d\Omega dz_s dz_l} \right) (1+z_s) + \left[\frac{\partial \theta_E}{\partial r_s \mathcal{H}(z'_s)} + 1 \right] \frac{dN}{d\Omega dz_s dz_l} = \frac{\partial}{\partial z_s} \left[\frac{dN}{d\Omega dz_s dz_l} (1+z_s) \theta_E \right] \quad (\text{A.10})$$

we obtain

$$\begin{aligned} &\int dz'_s \int dz'_l \theta'_E(\hat{\mathbf{n}}', z'_s, z'_l) \frac{dN(z'_s, z'_l, \hat{\mathbf{n}}')}{d\Omega' dz'_s dz'_l} \\ &= \int dz'_s \int dz'_l \frac{dN(r(z'_s), r(z'_l))}{d\Omega dz_s dz_l} \theta_E \left(1 + 2 \frac{v_o}{c} \cos \theta'_{\text{cm}} - \frac{v_o}{2c} \cos \theta'_{\text{cm}} \right) \\ &+ \int dz'_s \int dz'_l \left\{ \frac{\partial}{\partial z_s} \left[\frac{dN}{d\Omega dz_s dz_l} (1+z_s) \theta_E \right] + \frac{\partial}{\partial z_l} \left[\frac{dN}{d\Omega dz_s dz_l} (1+z_l) \theta_E \right] \right\} \frac{v_o}{c} \cos \theta'_{\text{cm}}. \end{aligned} \quad (\text{A.11})$$

The terms in the last line can directly be integrated, giving rise to boundary terms that exactly vanish since the number of rings at redshift 0 and at infinity is zero. The only effect that survives is therefore the effect of aberration, which modifies both the number of rings (second term in the second line of (A.11)) and the Einstein radius (third term in the second line of (A.11)). A similar calculation can be performed for the denominator of Eq. (2.9), $dN(\hat{\mathbf{n}}')/d\Omega'$, leading to

$$\frac{dN(\hat{\mathbf{n}}')}{d\Omega'} = \int dz'_s \int dz'_l \frac{dN(r(z'_s), r(z'_l))}{d\Omega dz_s dz_l} \theta_E \left(1 + 2 \frac{v_o}{c} \cos \theta'_{\text{cm}} \right). \quad (\text{A.12})$$

Taking the ratio of Eqs. (A.11) and (A.12), we obtain for the mean

$$\langle \theta'_E(\hat{\mathbf{n}}') \rangle = \left(1 - \frac{v_o}{2c} \cos \theta'_{\text{cm}} \right) \int dz'_s \int dz'_l f(z'_s, z'_l) \theta_E(z'_s, z'_l), \quad (\text{A.13})$$

with $f(z'_s, z'_l)$ given in Eq. (2.15).

B Impact of the selection function on the dipole

We compute here the impact of selection in flux and size on the dipole. We work in redshift space, but as we will see, we would obtain the same result using comoving distances, once the signal is integrated from 0 to ∞ .

The mean Einstein radius, averaged over sources with a flux larger than F'_* and a size larger than θ'_{E*} , is given by

$$\begin{aligned} \langle \theta'_E(\hat{\mathbf{n}}') \rangle &= \left(\frac{dN(\hat{\mathbf{n}}', \theta'_E > \theta'_{E*}, F' > F'_*)}{d\Omega'} \right)^{-1} \\ &\times \int dz'_s \int dz'_l \int_{\theta'_{E*}} d\theta'_E \frac{dN(\hat{\mathbf{n}}', z'_s, z'_l, \theta'_E, F' > F'_*)}{d\Omega' dz'_s dz'_l d\theta'_E} \theta'_E(\hat{\mathbf{n}}', z'_s, z'_l). \end{aligned} \quad (\text{B.1})$$

In principle, we could also add a threshold on the flux of the lens, but this is irrelevant since the vast majority of sources for which the ring is detected have a lens that is also detected.

The observed flux is related to the intrinsic source luminosity L through the luminosity distance

$$F' = \frac{L}{4\pi d_L^2}. \quad (\text{B.2})$$

The observed flux threshold F'_* is, by construction, independent of direction. However, since the luminosity distance depends on direction through the boost, the intrinsic luminosity threshold also depends on direction

$$L_*(r(z'_s)) + \delta L_*(\hat{\mathbf{n}}', z'_s) = 4\pi d_L^2 \left(1 + 2 \frac{\delta d_L}{d_L} \right) F'_* = 4\pi d_L^2 \left(1 + 2 \frac{v_o \cos \theta'_{\text{cm}}}{c \mathcal{H} r} \right) F'_*, \quad (\text{B.3})$$

where the luminosity distance fluctuation has been computed in [53]. We will therefore detect a different number of rings above the flux threshold in the direction of the boost than in the opposite direction. If this effect were independent of the distance, it would affect the numerator and the denominator of (B.1) in the same way, and it would cancel. However, as we will see, this is not the case, and there is a non-zero contribution.

Similarly to the flux, we can relate the observed Einstein radius to its intrinsic size (which depends only on the mass of the lens) by factoring out the dependence on angular diameter distances

$$\theta'_E = \theta_E^{\text{int}} \left(1 - \frac{v_o}{2c} \cos \theta'_{\text{cm}} \right) g(z'_s, z'_l), \quad (\text{B.4})$$

where $g(z'_s, z'_l) = d_{ls}(z'_s, z'_l)/d_s(z'_s)$. As for the luminosity, since the observed size threshold is independent of direction, the intrinsic size threshold acquires a dependence on $\hat{\mathbf{n}}'$ through the boost

$$\theta_{E*}^{\text{int}}(r(z'_s), r(z'_l)) + \delta \theta_{E*}^{\text{int}}(\hat{\mathbf{n}}', z'_s, z'_l) = \frac{\theta_{E*}^{\text{int}}}{g(r(z'_s), r(z'_l))} \left(1 + \frac{v_o}{2c} \cos \theta'_{\text{cm}} - \frac{\partial g}{\partial r_s} \frac{\delta r_s}{g} - \frac{\partial g}{\partial r_l} \frac{\delta r_l}{g} \right). \quad (\text{B.5})$$

We then have

$$\int_{\theta'_{E*}} d\theta'_E \frac{dN(\hat{\mathbf{n}}', z'_s, z'_l, \theta'_E, F' > F'_*)}{d\Omega' dz'_s dz'_l d\theta'_E} \theta'_E = \int_{\theta_{E*}^{\text{int}} + \delta \theta_{E*}^{\text{int}}} d\theta_E^{\text{int}} \frac{dN(\hat{\mathbf{n}}', z'_s, z'_l, \theta_E^{\text{int}}, L > L_* + \delta L_*)}{d\Omega' dz'_s dz'_l d\theta_E^{\text{int}}} \theta_E^{\text{int}}$$

$$\begin{aligned}
&= \int_{\theta_{E*}^{\text{int}}} d\theta_E^{\text{int}} \theta_E^{\text{int}} \left\{ \frac{dN(r(z'_s), r(z'_l), \theta_E^{\text{int}}, L > L_*)}{d\Omega dz_s dz_l d\theta_E^{\text{int}}} g(r(z'_s), r(z'_l)) \left(1 + \frac{3}{2} \frac{v_o}{c} \cos \theta'_{\text{cm}} \right) \right. \\
&\quad + \frac{\partial}{\partial z'_s} \left[\frac{dN(r(z'_s), r(z'_l), \theta_E^{\text{int}}, L > L_*)}{d\Omega dz_s dz_l d\theta_E^{\text{int}}} (1 + z'_s) g(r(z'_s), r(z'_l)) \right] \frac{v_o}{c} \cos \theta'_{\text{cm}} \\
&\quad + \frac{\partial}{\partial z'_l} \left[\frac{dN(r(z'_s), r(z'_l), \theta_E^{\text{int}}, L > L_*)}{d\Omega dz_s dz_l d\theta_E^{\text{int}}} (1 + z'_l) g(r(z'_s), r(z'_l)) \right] \frac{v_o}{c} \cos \theta'_{\text{cm}} \\
&\quad + \left. \frac{\partial}{\partial L_*} \left[\frac{dN(r(z'_s), r(z'_l), \theta_E^{\text{int}}, L > L_*)}{d\Omega dz_s dz_l d\theta_E^{\text{int}}} \right] g(r(z'_s), r(z'_l)) \delta L_* \right\} \\
&\quad + \frac{\partial}{\partial \theta_{E*}^{\text{int}}} \left[\int_{\theta_{E*}^{\text{int}}} d\theta_E^{\text{int}} \theta_E^{\text{int}} \frac{dN(r(z'_s), r(z'_l), \theta_E^{\text{int}}, L > L_*)}{d\Omega dz_s dz_l d\theta_E^{\text{int}}} g(r(z'_s), r(z'_l)) \right] \delta \theta_{E*}^{\text{int}}. \tag{B.6}
\end{aligned}$$

As in the case without threshold effects in Appendix A, we want to group the terms in a total derivative that vanishes at the boundary. The difference here is that both L_* and θ_{E*}^{int} depend on redshifts. L_* depends only on the redshift of the source, while θ_{E*}^{int} depends on both redshifts. As a consequence, the total derivative acquires additional terms. More precisely the total derivative over z'_s is given by

$$\begin{aligned}
&\frac{d}{dz'_s} \left\{ \int_{\theta_{E*}^{\text{int}}} d\theta_E^{\text{int}} \theta_E^{\text{int}} \frac{dN(r(z'_s), r(z'_l), \theta_E^{\text{int}}, L > L_*)}{d\Omega dz_s dz_l d\theta_E^{\text{int}}} (1 + z'_s) g(r(z'_s), r(z'_l)) \right\} \frac{v_o}{c} \cos \theta'_{\text{cm}} \tag{B.7} \\
&= \int_{\theta_{E*}^{\text{int}}} d\theta_E^{\text{int}} \theta_E^{\text{int}} \left\{ \frac{\partial}{\partial z'_s} \left[\frac{dN(r(z'_s), r(z'_l), \theta_E^{\text{int}}, L > L_*)}{d\Omega dz_s dz_l d\theta_E^{\text{int}}} (1 + z'_s) g(r(z'_s), r(z'_l)) \right] \right. \\
&\quad + \frac{\partial}{\partial L_*} \left[\frac{dN(r(z'_s), r(z'_l), \theta_E^{\text{int}}, L > L_*)}{d\Omega dz_s dz_l d\theta_E^{\text{int}}} \right] g(r(z'_s), r(z'_l)) (1 + z'_s) \frac{dL_*}{dz'_s} \left. \right\} \frac{v_o}{c} \cos \theta'_{\text{cm}} \\
&\quad + \frac{\partial}{\partial \theta_{E*}^{\text{int}}} \left[\int_{\theta_{E*}^{\text{int}}} d\theta_E^{\text{int}} \theta_E^{\text{int}} \frac{dN(r(z'_s), r(z'_l), \theta_E^{\text{int}}, L > L_*)}{d\Omega dz_s dz_l d\theta_E^{\text{int}}} \right] g(r(z'_s), r(z'_l)) (1 + z'_s) \frac{d\theta_{E*}^{\text{int}}}{dz'_s} \frac{v_o}{c} \cos \theta'_{\text{cm}}.
\end{aligned}$$

A similar expression can be derived for z'_l , without the contribution from the third line since L_* , which is the intrinsic luminosity of the source, does not depend on the redshift of the lens. Using Eq. (B.7) in Eq. (B.6) and integrating over redshifts, we find

$$\begin{aligned}
&\int dz'_s \int dz'_l \int_{\theta_{E*}'} d\theta'_E \frac{dN(\hat{\mathbf{n}}', z'_s, z'_l, \theta'_E, F' > F'_*)}{d\Omega' dz'_s dz'_l d\theta'_E} \theta'_{E'}(\hat{\mathbf{n}}', z'_s, z'_l) \tag{B.8} \\
&= \int dz'_s \int dz'_l \left\{ \int_{\theta_{E*}^{\text{int}}} d\theta_E^{\text{int}} \theta_E^{\text{int}} \left[\frac{dN(r(z'_s), r(z'_l), \theta_E^{\text{int}}, L > L_*)}{d\Omega dz_s dz_l d\theta_E^{\text{int}}} g(r(z'_s), r(z'_l)) \left(1 + \frac{3}{2} \frac{v_o}{c} \cos \theta'_{\text{cm}} \right) \right. \right. \\
&\quad + \frac{\partial}{\partial L_*} \left(\frac{dN(r(z'_s), r(z'_l), \theta_E^{\text{int}}, L > L_*)}{d\Omega dz_s dz_l d\theta_E^{\text{int}}} \right) g(r(z'_s), r(z'_l)) \left(\delta L_* - (1 + z'_s) \frac{dL_*}{dz'_s} \frac{v_o}{c} \cos \theta'_{\text{cm}} \right) \left. \right] \\
&\quad + \frac{\partial}{\partial \theta_{E*}^{\text{int}}} \left(\int_{\theta_{E*}^{\text{int}}} d\theta_E^{\text{int}} \theta_E^{\text{int}} \frac{dN(r(z'_s), r(z'_l), \theta_E^{\text{int}}, L > L_*)}{d\Omega dz_s dz_l d\theta_E^{\text{int}}} \right) \\
&\quad \times g(r(z'_s), r(z'_l)) \left[\delta \theta_{E*}^{\text{int}} - \left((1 + z'_s) \frac{d\theta_{E*}^{\text{int}}}{dz'_s} + (1 + z'_l) \frac{d\theta_{E*}^{\text{int}}}{dz'_l} \right) \frac{v_o}{c} \cos \theta'_{\text{cm}} \right] \left. \right\},
\end{aligned}$$

where we have used that the total derivatives over z'_s and z'_l cancel when integrated over all redshifts, since the number of rings at redshift 0 and infinity is zero. The luminosity perturbation and its redshift derivative can be directly computed from Eq. (B.3)

$$\delta L_* = \frac{2L_* v_o}{\mathcal{H}r} \cos \theta'_{\text{cm}}, \quad (\text{B.9})$$

$$(1 + z'_s) \frac{dL_*}{dz'_s} = 2L_* \left(1 + \frac{1}{r_s \mathcal{H}} \right). \quad (\text{B.10})$$

Similarly, the intrinsic size perturbation and its redshift derivatives can be computed from Eq. (B.5)

$$\delta \theta_{E*}^{\text{int}} = \theta_{E*}^{\text{int}} \left(\frac{v_o}{2c} \cos \theta'_{\text{cm}} - \frac{\partial g}{\partial r_s} \frac{\delta r_s}{g} - \frac{\partial g}{\partial r_l} \frac{\delta r_l}{g} \right), \quad (\text{B.11})$$

$$(1 + z'_s) \frac{d\theta_{E*}^{\text{int}}}{dz'_s} + (1 + z'_l) \frac{d\theta_{E*}^{\text{int}}}{dz'_l} = -\frac{\theta_{E*}^{\text{int}}}{g} \left(\frac{\partial g}{\partial z'_s} + \frac{\partial g}{\partial z'_l} \right). \quad (\text{B.12})$$

With this, Eq. (B.7) becomes

$$\begin{aligned} & \int dz'_s \int dz'_l \int_{\theta'_{E*}} d\theta'_E \frac{dN(\hat{\mathbf{n}}', z'_s, z'_l, \theta'_E, F' > F'_*)}{d\Omega' dz'_s dz'_l d\theta'_E} \theta'_E(\hat{\mathbf{n}}', z'_s, z'_l) \\ &= \int dz'_s \int dz'_l \int_{\theta_{E*}^{\text{int}}} d\theta_{E*}^{\text{int}} \theta_{E*}^{\text{int}} \left[\frac{dN(r(z'_s), r(z'_l), \theta_{E*}^{\text{int}}, L > L_*)}{d\Omega dz'_s dz'_l d\theta_{E*}^{\text{int}}} g(r(z'_s), r(z'_l)) \left(1 + \frac{3}{2} \frac{v_o}{c} \cos \theta'_{\text{cm}} \right) \right. \\ & \quad \left. - 2 \frac{\partial}{\partial L_*} \left(\frac{dN(r(z'_s), r(z'_l), \theta_{E*}^{\text{int}}, L > L_*)}{d\Omega dz'_s dz'_l d\theta_{E*}^{\text{int}}} \right) g(r(z'_s), r(z'_l)) L_* \frac{v_o}{c} \cos \theta'_{\text{cm}} \right] \\ & \quad - \int dz'_s \int dz'_l \theta_{E*}^{\text{int}} \frac{dN(r(z'_s), r(z'_l), \theta_{E*}^{\text{int}}, L > L_*)}{d\Omega dz'_s dz'_l d\theta_{E*}^{\text{int}}} g(r(z'_s), r(z'_l)) \theta_{E*}^{\text{int}} \frac{v_o}{2c} \cos \theta'_{\text{cm}}. \end{aligned} \quad (\text{B.13})$$

The last two lines are new contributions generated by the threshold effects: since the boost impacts the observed flux and the observed size of the Einstein ring, we see a different number of events in the direction of the boost and in the opposite direction, which impacts the integral over redshifts.

To obtain the mean Einstein radius, we need, however, to divide Eq. (B.13) by the number of events observed in the direction $\hat{\mathbf{n}}'$. Following the same steps as for Eq. (B.13), we find

$$\begin{aligned} & \frac{dN(\hat{\mathbf{n}}', \theta'_E > \theta'_{E*}, F' > F'_*)}{d\Omega'} \\ &= \int dz'_s \int dz'_l \int_{\theta_{E*}^{\text{int}}} d\theta_{E*}^{\text{int}} \left[\frac{dN(r(z'_s), r(z'_l), \theta_{E*}^{\text{int}}, L > L_*)}{d\Omega dz'_s dz'_l d\theta_{E*}^{\text{int}}} \left(1 + 2 \frac{v_o}{c} \cos \theta'_{\text{cm}} \right) \right. \\ & \quad \left. - 2 \frac{\partial}{\partial L_*} \left(\frac{dN(r(z'_s), r(z'_l), \theta_{E*}^{\text{int}}, L > L_*)}{d\Omega dz'_s dz'_l d\theta_{E*}^{\text{int}}} \right) L_* \frac{v_o}{c} \cos \theta'_{\text{cm}} \right] \\ & \quad - \int dz'_s \int dz'_l \frac{dN(r(z'_s), r(z'_l), \theta_{E*}^{\text{int}}, L > L_*)}{d\Omega dz'_s dz'_l d\theta_{E*}^{\text{int}}} \theta_{E*}^{\text{int}} \frac{v_o}{2c} \cos \theta'_{\text{cm}}. \end{aligned} \quad (\text{B.14})$$

We then rewrite Eqs. (B.13) and (B.14) in terms of the Einstein radius $\theta_E = g(r(z'_s), r(z'_l)) \theta_{E*}^{\text{int}}$, and we take the ratio. This gives the final result

$$\langle \theta'_E \rangle = \langle \theta_E \rangle \left(1 - \frac{v_o}{2c} \cos \theta'_{\text{cm}} \right) \quad (\text{B.15})$$

$$\begin{aligned}
& + 2 \frac{v_o}{c} \cos \theta'_{\text{cm}} \int dz'_s \int_{\theta_{E*}} d\theta_E (\theta_E - \langle \theta_E \rangle) f_1(z'_s, \theta_E, L > L_*) x(z'_s, \theta_E, L_*) \\
& + \frac{v_o}{2c} \cos \theta'_{\text{cm}} (\langle \theta_E \rangle - \theta_{E*}) \int dz'_s \int dz'_l f_2(z'_s, z'_l, \theta_E > \theta_{E*}, L > L_*) \mu(z'_s, z'_l, \theta_{E*}, L_*).
\end{aligned}$$

Here f_1 is the distribution of systems, already integrated over the redshifts of the lenses (which do not impact the flux threshold)

$$f_1(z'_s, \theta_E, L > L_*) = \left(\frac{dN(\theta_E > \theta_{E*}, L > L_*)}{d\Omega} \right)^{-1} \frac{dN(r(z'_s), \theta_E, L > L_*)}{d\Omega dz_s d\theta_E}, \quad (\text{B.16})$$

and f_2 is the cumulative distribution with sizes above the threshold

$$f_2(z'_s, z'_l, \theta_E > \theta_{E*}, L > L_*) = \left(\frac{dN(\theta_E > \theta_{E*}, L > L_*)}{d\Omega} \right)^{-1} \frac{dN(r(z'_s), r(z'_l), \theta_E > \theta_{E*}, L > L_*)}{d\Omega dz_s dz_l}. \quad (\text{B.17})$$

These two distributions are unboosted quantities, which depend on the unboosted distance r , the unboosted angle θ_E , and the intrinsic unboosted luminosity threshold L_* . In practice, however, to predict the amplitude of the second and third lines in Eq. (B.15), we can directly use the measured mean redshift distribution as a function of the observed redshifts, the observed angle θ'_E , and the observed flux threshold $F' > F'_*$, since f_1 and f_2 multiply already v_o/c .

The second line in Eq. (B.15) encodes the impact of the flux threshold on the mean Einstein ring. It depends on the so-called (relativistic) magnification bias, i.e., the slope of the cumulative number of systems with a flux larger than the flux threshold

$$x(z'_s, \theta_E, L_*) \equiv - \frac{\partial \ln}{\partial \ln L_*} \left(\frac{dN(r(z'_s), \theta_E, L > L_*)}{d\Omega dz_s d\theta_E} \right) = - \frac{\partial \ln}{\partial \ln F'_*} \left(\frac{dN(z'_s, \theta'_E, F' > F'_*)}{d\Omega dz'_s d\theta'_E} \right), \quad (\text{B.18})$$

where in the second equality we have used the fact that x already multiplies v_o/c .

Finally, the third line in Eq. (B.15) encodes the impact of the size threshold. It depends on the slope of the cumulative number of systems with a size larger than θ_{E*}

$$\mu(z'_s, z'_l, \theta_{E*}, L_*) \equiv - \frac{\partial \ln}{\partial \ln \theta_{E*}} \left(\frac{dN(r(z'_s), r(z'_l), \theta_E > \theta_{E*}, L > L_*)}{d\Omega dz_s dz_l} \right). \quad (\text{B.19})$$

As for the magnification bias, unboosted quantities can be replaced by the measured ones in the definition of μ .

C Simulation of the Fundamental Plane observables

We define the FP logarithmic variables:

$$\mathbf{x} \equiv (r, s, i) \equiv (\log R_e, \log \sigma_{\text{FP}}, \log I_e), \quad (\text{C.1})$$

and we model the intrinsic distribution of galaxies as a tri-variate Gaussian, following e.g. [54]:

$$P(\mathbf{x}) = \mathcal{N}(\boldsymbol{\mu}, \boldsymbol{\Sigma}), \quad (\text{C.2})$$

with mean

$$\boldsymbol{\mu} = (\bar{r}, \bar{s}, \bar{i}), \quad (\text{C.3})$$

and covariance matrix $\boldsymbol{\Sigma}$.

The covariance matrix is constructed from the orthonormal eigenbasis:

$$\{\hat{\mathbf{u}}_1, \hat{\mathbf{u}}_2, \hat{\mathbf{n}}\}, \quad (\text{C.4})$$

where $\hat{\mathbf{u}}_1$ and $\hat{\mathbf{u}}_2$ span the FP and $\hat{\mathbf{n}}$ is perpendicular to it. The unit vector perpendicular to the FP, $\hat{\mathbf{n}}$, can be related to the cartesian basis $(\hat{\mathbf{e}}_r, \hat{\mathbf{e}}_s, \hat{\mathbf{e}}_i)$:

$$\hat{\mathbf{n}} = \frac{-a\hat{\mathbf{e}}_r + \hat{\mathbf{e}}_s - b\hat{\mathbf{e}}_i}{\sqrt{a^2 + b^2 + 1}}. \quad (\text{C.5})$$

In this basis, the intrinsic dispersions are $(\sigma_1, \sigma_2, \sigma_3)$, with σ_3 being the thickness of the FP. The covariance matrix is then

$$\boldsymbol{\Sigma}_{rsi} = \mathbf{V} \begin{pmatrix} \sigma_1^2 & 0 & 0 \\ 0 & \sigma_2^2 & 0 \\ 0 & 0 & \sigma_3^2 \end{pmatrix} \mathbf{V}^\top, \quad (\text{C.6})$$

where $\mathbf{V} = (\hat{\mathbf{u}}_1, \hat{\mathbf{u}}_2, \hat{\mathbf{n}})$. For each lens of our sample, the conditional distribution of (r, i) , given the true value s , remains Gaussian:

$$P(r, i | s) = \mathcal{N}(\boldsymbol{\mu}_{RI|s}, \boldsymbol{\Sigma}_{RI|s}), \quad (\text{C.7})$$

with conditional mean

$$\boldsymbol{\mu}_{ri|s} = \boldsymbol{\mu}_{ri} + \boldsymbol{\Sigma}_{ri,s} \boldsymbol{\Sigma}_{ss}^{-1} (s - \bar{s}), \quad (\text{C.8})$$

and conditional covariance

$$\boldsymbol{\Sigma}_{RI|s} = \boldsymbol{\Sigma}_{RI} - \boldsymbol{\Sigma}_{RI,s} \boldsymbol{\Sigma}_{ss}^{-1} \boldsymbol{\Sigma}_{s,RI}, \quad (\text{C.9})$$

where $\boldsymbol{\Sigma}_{RI}$ is the 2×2 covariance of (r, i) , $\boldsymbol{\Sigma}_{RI,s}$ is the covariance between (r, i) and s , and $\boldsymbol{\Sigma}_{ss}$ is the variance of s

We emulate the measurement errors $(\delta r, \delta i)$ on the observable (r, i) for each lens system from a multivariate Gaussian distribution, following [55]:

$$\begin{pmatrix} \delta r \\ \delta i \end{pmatrix} \sim \mathcal{N}(0, \mathbf{E}_n), \quad \mathbf{E}_n = \begin{pmatrix} \epsilon_r^2 & \rho_{ri} \epsilon_r \epsilon_i \\ \rho_{ri} \epsilon_r \epsilon_i & \epsilon_i^2 \end{pmatrix}, \quad (\text{C.10})$$

where $\rho_{ri} = -0.95$ is the correlation between the photometric quantities r and i . ϵ_r and ϵ_i were found to be 0.049 dex (11%) and 0.073 dex (17%) in [44], from ground-based imaging. Although these could be substantially improved with Euclid [56], we adopt a conservative value of $\epsilon_r = 0.041$ dex (10%) and $\epsilon_i = 0.06$ dex (15%).

The observed quantities are

$$r_{\text{obs}} = r_{\text{true}} + \delta r, \quad i_{\text{obs}} = i_{\text{true}} + \delta i. \quad (\text{C.11})$$

Adopting the same tri-variate Gaussian model and defining the total covariance matrix $\mathbf{C}_n = \boldsymbol{\Sigma} + \mathbf{E}_n$. We can obtain an estimate of s given the observed $(r_{\text{obs}}, i_{\text{obs}})$

$$P(s | r, i) = \mathcal{N}(\mu_{s|RI}, \sigma_{s|RI}^2), \quad (\text{C.12})$$

with conditional mean

$$\mu_{s|RI} = \mu_s + \mathbf{C}_{s,RI} \mathbf{C}_{RI}^{-1} \left(\begin{pmatrix} r \\ i \end{pmatrix} - \boldsymbol{\mu}_{RI} \right) \quad (\text{C.13})$$

and conditional variance

$$\sigma_{s|RI}^2 = C_{ss} - \mathbf{C}_{s,RI} \mathbf{C}_{RI}^{-1} \mathbf{C}_{RI,s}, \quad (\text{C.14})$$

where we partitioned the mean vector and covariance matrix as follows

$$\boldsymbol{\mu} = \begin{pmatrix} \boldsymbol{\mu}_{RI} \\ \mu_s \end{pmatrix}, \quad \mathbf{C}_n = \begin{pmatrix} \mathbf{C}_{RI} & \mathbf{C}_{RI,s} \\ \mathbf{C}_{s,RI} & C_{ss} \end{pmatrix}, \quad \boldsymbol{\mu}_{RI} = (\bar{r}, \bar{i}). \quad (\text{C.15})$$

D Observer velocity effect on the Fundamental Plane observables

Here we describe how to use the FP relation (Eq. (4.13)) to estimate the velocity dispersion σ_{FP} , and in turn infer the boosted Einstein angle under the SIS assumption with $\sigma_v = \sigma_{\text{FP}}$. To this end, it is necessary to understand how the effective radius R_e and the mean surface brightness I_e transform under a Lorentz boost. The radius can be estimated from the subtended angle and the lens redshift via a cosmological model. The subtended angle is subject to aberration, and the angular diameter distance d_A is estimated from an observed redshift, which is Doppler shifted by v_o . The subtended angle α is affected on average as the Einstein angle (Eq. (2.8))

$$\alpha = \alpha' \left(1 + \frac{v_o}{2c} \cos(\theta'_{\text{cm}}) \right). \quad (\text{D.1})$$

The radius can be expressed as

$$R_e = \alpha d_A = \alpha' d[z'_l] \left(1 + \frac{v_o}{2c} \cos(\theta'_{\text{cm}}) + \frac{D_L}{d[z'_l]} \frac{v_o}{c} \right). \quad (\text{D.2})$$

In the following, we show that the mean surface brightness is invariant under a boost. It is defined as (Eq. (1.20) p.23 of [57])

$$I_e \equiv \frac{L}{2\pi R_e^2}, \quad (\text{D.3})$$

and is often quoted in [W pc^{-2}]. The luminosity L [W] can be computed from the flux $L = 4\pi d_L^2 F$ using the luminosity distance d_L [m] and the flux F [W m^{-2}], which can itself be computed from the specific intensity $I(\nu, \hat{\mathbf{n}})$ [$\text{W m}^{-2} \text{Hz}^{-1} \text{sr}^{-1}$] by integrating over frequency and solid angle over the relevant surface \mathcal{S}

$$F = \int_{\mathbb{R}_+} d\nu d^2 \int_{\mathcal{S}} \hat{\mathbf{n}} I(\nu, \hat{\mathbf{n}}) R(\nu). \quad (\text{D.4})$$

where $R(\nu)$ is a filter that can be taken to be a tophat. Combining these steps, one obtains

$$I_e = \frac{L}{2\pi R_e^2} = \frac{4\pi d_L^2 F}{2d_A^2 \Omega} = \frac{2\pi d_L^2}{d_A^2 \Omega} \int_{\mathbb{R}_+} d\nu \int_{\mathcal{S}} d^2 \hat{\mathbf{n}} I(\nu, \hat{\mathbf{n}}) R(\nu) \quad (\text{D.5})$$

where $\Omega = \pi\alpha^2$. We assume for simplicity that $I_\nu(\nu, \hat{\mathbf{n}})$ is constant across the relevant angles spanned by $\hat{\mathbf{n}} \in \mathcal{S}$, i.e., $I(\nu, \hat{\mathbf{n}}) = I(\nu)$. This leads to

$$I_e = \frac{2\pi d_L^2}{d_A^2} \int_{\mathbb{R}_+} d\nu I(\nu) R(\nu). \quad (\text{D.6})$$

Using Etherington's reciprocity law $d_L = (1 + z_l)^2 d_A$ [58], we obtain the simple expression

$$I_e = 2\pi(1 + z_l)^4 \int_{\mathbb{R}_+} d\nu I(\nu) R(\nu). \quad (\text{D.7})$$

One can use the following transformation properties

$$I(\nu, \hat{\mathbf{n}}) = I'(\nu', \hat{\mathbf{n}}') \left(\frac{\nu}{\nu'}\right)^3, \quad (\text{D.8})$$

$$(1 + z_l) = (1 + z'_l) \left(1 + Z_L \frac{v_o}{c}\right), \quad (\text{D.9})$$

$$\nu = \frac{\nu}{\nu_s} \frac{\nu_s}{\nu'} \nu' = \frac{(1 + z'_l)}{(1 + z_l)} \nu' = \nu' \left(1 - Z_L \frac{v_o}{c}\right), \quad (\text{D.10})$$

where Z_L was defined in Eq. (4.5) in terms of the observer's lens and source peculiar velocities, and the identity for the specific intensity follows from the fact that I/ν^3 is a Lorentz invariant. Combining these, the mean surface brightness transforms as

$$I_e = 2\pi(1 + z_l)^4 \int_{R_+} d\nu I(\nu) R(\nu) \quad (\text{D.11})$$

$$\begin{aligned} &= 2(1 + z'_l)^4 \left(1 + 4Z_L \frac{v_o}{c}\right) \int_{R_+} d\nu' \left(1 - Z_L \frac{v_o}{c}\right) I'(\nu') \left(\frac{\nu}{\nu'}\right)^3 R(\nu') \\ &= 2\pi(1 + z'_l)^4 \left(1 + 4Z_L \frac{v_o}{c}\right) \left(1 - 4Z_L \frac{v_o}{c}\right) \int_{R_+} d\nu' I'(\nu') R(\nu') \\ &= 2\pi(1 + z'_l)^4 \int_{R_+} d\nu' I'(\nu') R(\nu') \\ &= I'_e. \end{aligned} \quad (\text{D.12})$$

Hence, the mean surface brightness is invariant under a boost. Hence, σ_v is affected by the boost only via R_e . We obtain

$$\begin{aligned} a \log \sigma_v &= \log R_e - b \log I_e - c \\ &= \log(\alpha' d[z'_l]) - b \log(I'_e) - c + \log \left(1 + \frac{1}{2} \mathbf{v}_o \cdot \hat{\mathbf{n}}' + \frac{D_L}{d[z'_l]} \frac{v_o}{c}\right). \end{aligned} \quad (\text{D.13})$$

Explicitly, the velocity dispersion σ_v can be expressed as

$$\sigma_v = \sigma'_v \left(1 + \Sigma_v \frac{v_o}{c}\right), \quad (\text{D.14})$$

with the naive σ'_v , which would be extracted from observables if we didn't account for the peculiar velocities and the correction Σ_v defined as

$$\sigma'_v = \left(10^{-c} \alpha' d[z'_l] (I'_e)^{-b}\right)^{1/a}, \quad (\text{D.15})$$

$$\Sigma_v = \left(\frac{1}{2a} \cos(\theta'_{\text{cm}}) + \frac{D_L}{ad[z'_l]} \right). \quad (\text{D.16})$$

We can further compute the effect on the Einstein angle if one assumes that $\sigma_v = \sigma_{\text{FP}}$ and adopts the SIS assumption

$$\theta'_{E,\text{FP}} = \frac{4\pi\sigma_v^2}{c^2} \frac{d_{ls}}{d_s} = \frac{4\pi\sigma_v^2}{c^2} \frac{d[z'_l, z'_s]}{d[z'_s]} \left(1 + \frac{D_{LS}}{d[z'_l, z'_s]} \frac{v_o}{c} - \frac{D_S}{d[z'_s]} \frac{v_o}{c} + 2\Sigma_v \frac{v_o}{c} \right) \quad (\text{D.17})$$

Replacing this expression for the Einstein angle in Eq. (2.8), we get

$$\theta'_{E,\text{FP}} = \frac{4\pi\sigma_v^2}{c^2} \frac{d[z'_l, z'_s]}{d[z'_s]} \left(1 - \frac{1}{2} \frac{v_o}{c} \cos(\theta'_{\text{cm}}) + \frac{D_{LS}}{d[z'_l, z'_s]} \frac{v_o}{c} - \frac{D_S}{d[z'_s]} \frac{v_o}{c} + 2\Sigma_v \frac{v_o}{c} \right). \quad (\text{D.18})$$

This expression can be used to infer v_o from the observables $z'_l, z'_s, \alpha', I'_e, \theta'_{\text{cm}}$, and the FP parameters a, b, c , which we assume are not affected by the boost. This is the expression that appears in (4.15).

References

- [1] D. J. Fixsen, E. S. Cheng, D. A. Cottingham, J. Eplee, R. E., R. B. Isaacman, J. C. Mather, S. S. Meyer, P. D. Noerdlinger, R. A. Shafer, R. Weiss, E. L. Wright, C. L. Bennett, N. W. Boggess, T. Kelsall, S. H. Moseley, R. F. Silverberg, G. F. Smoot, and D. T. Wilkinson, *Cosmic Microwave Background Dipole Spectrum Measured by the COBE FIRAS Instrument*, *ApJ* **420** (Jan., 1994) 445.
- [2] D. J. Fixsen, E. S. Cheng, J. M. Gales, J. C. Mather, R. A. Shafer, and E. L. Wright, *The Cosmic Microwave Background spectrum from the full COBE FIRAS data set*, *Astrophys. J.* **473** (1996) 576, [[astro-ph/9605054](#)].
- [3] **Planck** Collaboration, N. Aghanim et al., *Planck 2018 results. VI. Cosmological parameters*, *Astron. Astrophys.* **641** (2020) A6, [[arXiv:1807.06209](#)].
- [4] **Planck** Collaboration, N. Aghanim et al., *Planck 2013 results. XXVII. Doppler boosting of the CMB: Eppur si muove*, *Astron. Astrophys.* **571** (2014) A27, [[arXiv:1303.5087](#)].
- [5] P. d. S. Ferreira and M. Quartin, *First Constraints on the Intrinsic CMB Dipole and Our Velocity with Doppler and Aberration*, *Phys. Rev. Lett.* **127** (2021), no. 10 101301, [[arXiv:2011.08385](#)].
- [6] S. Saha, S. Shaikh, S. Mukherjee, T. Souradeep, and B. D. Wandelt, *Bayesian estimation of our local motion from the Planck-2018 CMB temperature map*, *JCAP* **10** (2021) 072, [[arXiv:2106.07666](#)].
- [7] D. J. Schwarz, C. J. Copi, D. Huterer, and G. D. Starkman, *CMB anomalies after planck*, *Classical and Quantum Gravity* **33** (aug, 2016) 184001.
- [8] G. F. R. Ellis and J. E. Baldwin, *On the expected anisotropy of radio source counts*, *MNRAS* **206** (Jan., 1984) 377–381.
- [9] N. J. Secrest, S. v. Hausegger, M. Rameez, R. Mohayaee, S. Sarkar, and J. Colin, *A test of the cosmological principle with quasars*, *The Astrophysical Journal* **908** (Feb, 2021) L51.
- [10] L. Dam, G. F. Lewis, and B. J. Brewer, *Testing the Cosmological Principle with CatWISE Quasars: A Bayesian Analysis of the Number-Count Dipole*, [[arXiv:2212.07733](#)].
- [11] N. Secrest, S. von Hausegger, M. Rameez, R. Mohayaee, and S. Sarkar, *A Challenge to the Standard Cosmological Model*, [[arXiv:2206.05624](#)].

- [12] O. T. Oayda, V. Mittal, G. F. Lewis, and T. Murphy, *A Bayesian approach to the cosmic dipole in radio galaxy surveys: joint analysis of NVSS & RACS*, *MNRAS* **531** (July, 2024) 4545–4559, [[arXiv:2406.01871](#)].
- [13] C. Dalang and C. Bonvin, *On the kinematic cosmic dipole tension*, *Mon. Not. Roy. Astron. Soc.* **512** (2022), no. 3 3895–3905, [[arXiv:2111.03616](#)].
- [14] S. von Hausegger, *The expected kinematic matter dipole is robust against source evolution*, *Mon. Not. Roy. Astron. Soc.* **535** (2024), no. 1 L49–L53, [[arXiv:2404.07929](#)].
- [15] K. Storey-Fisher, D. W. Hogg, H.-W. Rix, A.-C. Eilers, G. Fabbian, M. R. Blanton, and D. Alonso, *Quaia, the Gaia-unWISE Quasar Catalog: An All-sky Spectroscopic Quasar Sample*, *ApJ* **964** (Mar., 2024) 69, [[arXiv:2306.17749](#)].
- [16] V. Mittal, O. T. Oayda, and G. F. Lewis, *The cosmic dipole in the Quaia sample of quasars: a Bayesian analysis*, *MNRAS* **527** (Jan., 2024) 8497–8510, [[arXiv:2311.14938](#)].
- [17] A. Abghari, E. F. Bunn, L. T. Hergt, B. Li, D. Scott, R. M. Sullivan, and D. Wei, *Reassessment of the dipole in the distribution of quasars on the sky*, *JCAP* **2024** (Nov., 2024) 067, [[arXiv:2405.09762](#)].
- [18] M. Bashir, P. Chingangbam, and S. Appleby, *The CatWISE2020 Quasar dipole: A Reassessment of the Cosmic Dipole Anomaly*, *arXiv e-prints* (Nov., 2025) arXiv:2511.00822, [[arXiv:2511.00822](#)].
- [19] S. von Hausegger and C. Dalang, *Redshift tomography of the kinematic matter dipole*, *Phys. Rev. D* **111** (2025), no. 12 123547, [[arXiv:2412.13162](#)].
- [20] F. Lacasa, C. Bonvin, C. Dalang, and R. Durrer, *Fast and spurious: a robust determination of our peculiar velocity with future galaxy surveys*, *JCAP* **06** (2024) 045, [[arXiv:2402.18438](#)].
- [21] N. J. Secrest, *The Ellis-Baldwin test*, *Philosophical Transactions of the Royal Society of London Series A* **383** (Feb., 2025) 20240027.
- [22] N. Secrest, S. von Hausegger, M. Rameez, R. Mohayaee, and S. Sarkar, *Colloquium: The Cosmic Dipole Anomaly*, *arXiv e-prints* (May, 2025) arXiv:2505.23526, [[arXiv:2505.23526](#)].
- [23] **Euclid** Collaboration, M. Walmsley et al., *Euclid Quick Data Release (Q1): The Strong Lensing Discovery Engine A – System overview and lens catalogue*, *arXiv e-prints* (Mar., 2025) arXiv:2503.15324, [[arXiv:2503.15324](#)].
- [24] **Euclid** Collaboration, K. Rojas et al., *Euclid Quick Data Release (Q1) The Strong Lensing Discovery Engine B – Early strong lens candidates from visual inspection of high velocity dispersion galaxies*, *arXiv e-prints* (Mar., 2025) arXiv:2503.15325, [[arXiv:2503.15325](#)].
- [25] **Euclid** Collaboration, N. E. P. Lines et al., *Euclid Quick Data Release (Q1). The Strong Lensing Discovery Engine C: Finding lenses with machine learning*, *arXiv e-prints* (Mar., 2025) arXiv:2503.15326, [[arXiv:2503.15326](#)].
- [26] **Euclid** Collaboration, P. Holloway et al., *Euclid Quick Data Release (Q1). The Strong Lensing Discovery Engine E – Ensemble classification of strong gravitational lenses: lessons for Data Release 1*, *arXiv e-prints* (Mar., 2025) arXiv:2503.15328, [[arXiv:2503.15328](#)].
- [27] M. Sereno, *Aberration in gravitational lensing*, *Phys. Rev. D* **78** (Oct., 2008) 083003, [[arXiv:0809.3900](#)].
- [28] C. Dalang, M. Millon, and T. Baker, *Peculiar velocity effects on the Hubble constant from time-delay cosmography*, *Phys. Rev. D* **107** (June, 2023) 123528, [[arXiv:2301.05574](#)].
- [29] A. Dressler, D. Lynden-Bell, D. Burstein, R. L. Davies, S. M. Faber, R. Terlevich, and G. Wegner, *Spectroscopy and Photometry of Elliptical Galaxies. I. New Distance Estimator*, *ApJ* **313** (Feb., 1987) 42.

- [30] S. Djorgovski and M. Davis, *Fundamental Properties of Elliptical Galaxies*, *ApJ* **313** (Feb., 1987) 59.
- [31] T. E. Collett, “LensPop: Galaxy-galaxy strong lensing population simulation.” Astrophysics Source Code Library, record ascl:1705.009, May, 2017.
- [32] T. E. Collett, *The Population of Galaxy-Galaxy Strong Lenses in Forthcoming Optical Imaging Surveys*, *ApJ* **811** (Sept., 2015) 20, [[arXiv:1507.02657](https://arxiv.org/abs/1507.02657)].
- [33] C. Park, Y.-Y. Choi, M. S. Vogeley, J. R. Gott, III, M. R. Blanton, and SDSS Collaboration, *Environmental Dependence of Properties of Galaxies in the Sloan Digital Sky Survey*, *ApJ* **658** (Apr., 2007) 898–916, [[astro-ph/0611610](https://arxiv.org/abs/astro-ph/0611610)].
- [34] A. J. Connolly, J. Peterson, J. G. Jernigan, R. Abel, J. Bankert, C. Chang, C. F. Claver, R. Gibson, D. K. Gilmore, E. Grace, R. L. Jones, Z. Ivezić, J. Jee, M. Juric, S. M. Kahn, V. L. Krabbandam, S. Krughoff, S. Lorenz, J. Pizagno, A. Rasmussen, N. Todd, J. A. Tyson, and M. Young, *Simulating the LSST system*, in *Modeling, Systems Engineering, and Project Management for Astronomy IV* (G. Z. Angeli and P. Dierickx, eds.), vol. 7738 of *Society of Photo-Optical Instrumentation Engineers (SPIE) Conference Series*, p. 77381O, July, 2010.
- [35] G. De Lucia, V. Springel, S. D. M. White, D. Croton, and G. Kauffmann, *The formation history of elliptical galaxies*, *MNRAS* **366** (Feb., 2006) 499–509, [[astro-ph/0509725](https://arxiv.org/abs/astro-ph/0509725)].
- [36] J. A. Acevedo Barroso, C. M. O’Riordan, B. Clément, C. Tortora, T. E. Collett, F. Courbin, R. Gavazzi, R. B. Metcalf, V. Busillo, I. T. Andika, R. Cabanac, H. M. Courtois, J. Crook-Mansour, L. Delchambre, G. Despali, L. R. Ecker, A. Franco, P. Holloway, N. Jackson, K. Jahnke, G. Mahler, L. Marchetti, P. Matavulj, A. Melo, M. Meneghetti, L. A. Moustakas, O. Müller, A. A. Nucita, A. Paulino-Afonso, J. Pearson, K. Rojas, C. Scarlata, S. Schuldt, S. Serjeant, D. Sluse, S. H. Suyu, M. Vaccari, A. Verma, G. Varnardos, M. Walmsley, H. Bouy, G. L. Walth, D. M. Powell, M. Bolzonella, J.-C. Cuillandre, M. Kluge, T. Saifollahi, M. Schirmer, C. Stone, A. Acebron, L. Bazzanini, A. Díaz-Sánchez, N. B. Hogg, L. V. E. Koopmans, S. Kruk, L. Leuzzi, A. Manjón-García, F. Mannucci, B. C. Nagam, R. Pearce-Casey, L. Scharré, J. Wilde, B. Altieri, A. Amara, S. Andreon, N. Auricchio, C. Baccigalupi, M. Baldi, A. Balestra, S. Bardelli, A. Basset, P. Battaglia, R. Bender, D. Bonino, E. Branchini, M. Brescia, J. Brinchmann, A. Caillat, S. Camera, G. P. Candini, V. Capobianco, C. Carbone, J. Carretero, S. Casas, M. Castellano, G. Castignani, S. Cavuoti, A. Cimatti, C. Colodro-Conde, G. Congedo, C. J. Conselice, L. Conversi, Y. Copin, L. Corcione, M. Cropper, A. Da Silva, H. Degaudenzi, G. De Lucia, J. Dinis, F. Dubath, X. Dupac, S. Dusini, M. Farina, S. Farrens, S. Ferriol, M. Frailis, E. Franceschi, S. Galeotta, B. Garilli, K. George, W. Gillard, B. Gillis, C. Giocoli, P. Gómez-Alvarez, A. Grazian, F. Grupp, L. Guzzo, S. V. H. Haugan, H. Hoekstra, W. Holmes, I. Hook, F. Hormuth, A. Hornstrup, M. Jhabvala, B. Joachimi, E. Keihänen, S. Kermiche, A. Kiessling, B. Kubik, M. Kunz, H. Kurki-Suonio, D. Le Mignant, S. Ligi, P. B. Lilje, V. Lindholm, I. Lloro, G. Mainetti, E. Maiorano, O. Mansutti, S. Marcin, O. Marggraf, M. Martinelli, N. Martinet, F. Marulli, R. Massey, E. Medinaceli, M. Melchior, Y. Mellier, E. Merlin, G. Meylan, M. Moresco, L. Moscardini, E. Munari, R. Nakajima, C. Neissner, R. C. Nichol, S.-M. Niemi, J. W. Nightingale, C. Padilla, S. Paltani, F. Pasian, K. Pedersen, W. J. Percival, V. Pettorino, S. Pires, G. Polenta, M. Poncet, L. A. Popa, L. Pozzetti, F. Raison, R. Rebolo, A. Renzi, J. Rhodes, G. Riccio, E. Romelli, M. Roncarelli, E. Rossetti, R. Saglia, Z. Sakr, A. G. Sánchez, D. Sapone, P. Schneider, T. Schrabback, A. Secroun, G. Seidel, S. Serrano, C. Sirignano, G. Sirri, J. Skottfelt, L. Stanco, J. Steinwagner, P. Tallada-Crespí, D. Tavagnacco, A. N. Taylor, I. Tereno, R. Toledo-Moreo, F. Torradeflot, I. Tutusaus, E. A. Valentijn, and L. Valenziano, *Euclid: The Early Release Observations Lens Search Experiment*, *A&A* **697** (May, 2025) A14, [[arXiv:2408.06217](https://arxiv.org/abs/2408.06217)].
- [37] J. U. Lange, *nautilus: boosting Bayesian importance nested sampling with deep learning*, *Monthly Notices of the Royal Astronomical Society* **525** (08, 2023) 3181–3194, [<https://academic.oup.com/mnras/article-pdf/525/2/3181/51331635/stad2441.pdf>].

- [38] G. Cusin, C. Pitrou, C. Bonvin, A. Barrau, and K. Martineau, *Boosting gravitational waves: a review of kinematic effects on amplitude, polarization, frequency and energy density*, *Class. Quant. Grav.* **41** (2024), no. 22 225006, [[arXiv:2405.01297](#)].
- [39] S. Knabel, P. Mozumdar, A. J. Shajib, T. Treu, M. Cappellari, C. Spiniello, and S. Birrer, *TDCOSMO: XIX. Measuring stellar velocity dispersion with sub-percent accuracy for cosmography*, *A&A* **703** (Nov., 2025) A117, [[arXiv:2502.16034](#)].
- [40] **TDCOSMO** Collaboration, Tdcosmo Collaboration, S. Birrer, E. J. Buckley-Geer, M. Cappellari, F. Courbin, F. Dux, C. D. Fassnacht, J. A. Frieman, A. Galan, D. Gilman, X.-Y. Huang, S. Knabel, D. Langeroodi, H. Lin, M. Millon, T. Morishita, V. Motta, P. Mozumdar, E. Paic, A. J. Shajib, W. Sheu, D. Sluse, A. Sonnenfeld, C. Spiniello, M. Stiavelli, S. H. Suyu, C. Y. Tan, T. Treu, L. van de Vyvere, H. Wang, P. Wells, D. M. Williams, and K. C. Wong, *TDCOSMO 2025: Cosmological constraints from strong lensing time delays*, *A&A* **704** (Dec., 2025) A63, [[arXiv:2506.03023](#)].
- [41] T. E. Collett, A. Sonnenfeld, C. Frohmaier, K. Glazebrook, D. Sluse, V. Motta, A. Verma, T. Anguita, L. Koopmans, C. Tortora, F. Courbin, R. Cabanac, B. Frye, G. P. Smith, J. M. Diego, B. Alteiri, S. Lopez, C. Fassnacht, A. Cooray, A. Goobar, D. Rychanowski, S. Serjeant, J. Richard, T. Treu, L. Moustakas, R. Li, C. Jacobs, C. Lemon, L. Marchetti, P. Hartley, E. Jullo, C.-H. Lee, S. Birrer, A. Fritz, J. Nightingale, N. Napolitano, A. A. Plazas, S. Kruk, C. Spiniello, C. Grillo, S. Suyu, A. Shajib, G. Vernardos, S. Dye, T. Daylan, J. Newman, and S. Schuldt, *The 4MOST Strong Lensing Spectroscopic Legacy Survey (4SLS)*, *The Messenger* **190** (Mar., 2023) 49–52.
- [42] K. Said, C. Howlett, T. Davis, J. Lucey, C. Saulder, K. Douglass, A. G. Kim, A. Kremin, C. Ross, G. Aldering, J. N. Aguilar, S. Ahlen, S. BenZvi, D. Bianchi, D. Brooks, T. Claybaugh, K. Dawson, A. de la Macorra, B. Dey, P. Doel, K. Fanning, S. Ferraro, A. Font-Ribera, J. E. Forero-Romero, E. Gaztañaga, S. G. A. Gontcho, J. Guy, K. Honscheid, R. Kehoe, T. Kisner, A. Lambert, M. Landriau, L. Le Guillou, M. Manera, A. Meisner, R. Miquel, J. Moustakas, A. Muñoz-Gutiérrez, A. Myers, J. Nie, N. Palanque-Delabrouille, W. Percival, F. Prada, G. Rossi, E. Sanchez, D. Schlegel, M. Schubnell, J. H. Silber, D. Sprayberry, G. Tarlé, M. V. Magana, B. A. Weaver, R. Wechsler, Z. Zhou, and H. Zou, *DESI peculiar velocity survey – Fundamental Plane*, *MNRAS* **539** (June, 2025) 3627–3644, [[arXiv:2408.13842](#)].
- [43] R. Laureijs et al., *Euclid Science Requirements Document*, ESA Science Document DEM-SA-Dc-00001, European Space Agency, Mar., 2010. Issue 4.0, 5 March 2010.
- [44] C. Magoulas, C. M. Springob, M. Colless, D. H. Jones, L. A. Campbell, J. R. Lucey, J. Mould, T. Jarrett, A. Merson, and S. Brough, *The 6dF Galaxy Survey: the near-infrared Fundamental Plane of early-type galaxies*, *MNRAS* **427** (Nov., 2012) 245–273, [[arXiv:1206.0385](#)].
- [45] **DESI** Collaboration, DESI Collaboration, A. Aghamousa, et al., *The DESI Experiment Part I: Science, Targeting, and Survey Design*, *arXiv e-prints* (Oct., 2016) arXiv:1611.00036, [[arXiv:1611.00036](#)].
- [46] **4MOST** Collaboration, R. S. de Jong et al., *4MOST: Project overview and information for the First Call for Proposals*, *The Messenger* **175** (Mar., 2019) 3–11, [[arXiv:1903.02464](#)].
- [47] T. E. Collett and S. D. Cunningham, *Observational selection biases in time-delay strong lensing and their impact on cosmography*, *MNRAS* **462** (Nov., 2016) 3255–3264, [[arXiv:1605.08341](#)].
- [48] A. Sonnenfeld, *Statistical strong lensing. III. Inferences with complete samples of lenses*, *A&A* **659** (Mar., 2022) A132, [[arXiv:2109.13246](#)].
- [49] A. Sonnenfeld, S.-S. Li, G. Despali, R. Gavazzi, A. J. Shajib, and E. N. Taylor, *Strong lensing selection effects*, *A&A* **678** (Oct., 2023) A4, [[arXiv:2301.13230](#)].
- [50] A. Herle, C. M. O’Riordan, and S. Vegetti, *Selection functions of strong lens finding neural networks*, *MNRAS* **534** (Oct., 2024) 1093–1106, [[arXiv:2307.10355](#)].

- [51] P. Fleury, D. Johnson, T. Duboscq, N. B. Hogg, and J. Larena, *Cosmology with the line-of-sight shear of strong gravitational lenses*, *arXiv e-prints* (Mar., 2026) arXiv:2603.03441, [[arXiv:2603.03441](#)].
- [52] X. Huang, J. C. Inchausti, C. J. Storfer, S. Tabares-Tarquino, J. Moustakas, W. Sheu, S. Agarwal, M. Tamargo-Arizmendi, D. J. Schlegel, J. Aguilar, S. Ahlen, G. Aldering, S. Bailey, S. Banka, S. BenZvi, D. Bianchi, A. Bolton, D. Brooks, A. Cikota, T. Claybaugh, K. S. Dawson, A. de la Macorra, A. Dey, P. Doel, J. Edelman, J. E. Forero-Romero, E. Gaztanaga, S. G. A. Gontcho, A. X. Gonzalez-Morales, A. Gu, K. Honscheid, M. Ishak, S. Juneau, R. Kehoe, T. Kisner, S. E. Kopolov, K. J. Kwon, A. Lambert, M. Landriau, D. Lang, L. Le Guillou, M. E. Levi, J. Liu, A. Meisner, R. Miquel, A. D. Myers, S. Perlmutter, N. Palanque-Delabrouille, I. Perez-Rafols, C. Poppett, F. Prada, G. Rossi, D. Rubin, E. Sanchez, M. Schubnell, Y. Shu, E. Silver, D. Sprayberry, N. Suzuki, G. Tarle, B. A. Weaver, and H. Zou, *DESI Strong Lens Foundry II: DESI Spectroscopy for Strong Lens Candidates*, *arXiv e-prints* (Sept., 2025) arXiv:2509.18089, [[arXiv:2509.18089](#)].
- [53] C. Bonvin, R. Durrer, and M. A. Gasparini, *Fluctuations of the luminosity distance*, *Phys. Rev. D* **73** (2006) 023523, [[astro-ph/0511183](#)]. [Erratum: Phys.Rev.D 85, 029901 (2012)].
- [54] M. Colless, R. P. Saglia, D. Burstein, R. L. Davies, R. K. McMahan, and G. Wegner, *The peculiar motions of early-type galaxies in two distant regions - VII. Peculiar velocities and bulk motions*, *MNRAS* **321** (Feb., 2001) 277–305, [[astro-ph/0008418](#)].
- [55] K. Said, M. Colless, C. Magoulas, J. R. Lucey, and M. J. Hudson, *Joint analysis of 6dFGS and SDSS peculiar velocities for the growth rate of cosmic structure and tests of gravity*, *MNRAS* **497** (Sept., 2020) 1275–1293, [[arXiv:2007.04993](#)].
- [56] **Euclid** Collaboration, H. Bretonniere et al., *Euclid preparation. XXVI. The Euclid Morphology Challenge: Towards structural parameters for billions of galaxies*, *A&A* **671** (Mar., 2023) A102, [[arXiv:2209.12907](#)].
- [57] J. Binney and S. Tremaine, *Galactic Dynamics: Second Edition*. 2008.
- [58] I. M. H. Etherington, *LX. On the definition of distance in general relativity*, .